Draft version March 11, 2015
Preprint typeset using LaTeX style emulateapj v. 5/2/11

arXiv:1503.02756v1 [astro-ph.CO] 10 Mar 2015

ARE THE EFFECTS OF STRUCTURE FORMATION SEEN IN THE CENTRAL METALLICITY OF GALAXY CLUSTERS?

Tamer Y. Elkholy[1,2], Mark W. Bautz[2], Claude R. Canizares[1,2]

(Dated: March 11, 2015)
Draft version March 11, 2015

ABSTRACT

A sample of 46 nearby clusters observed with *Chandra* is analyzed to produce radial density, temperature, entropy and metallicity profiles, as well as other morphological measurements. The entropy profiles are computed to larger radial extents than in previous *Chandra* cluster sample analyses. We find that the iron mass fraction measured in the inner $0.15R_{500}$ shows a larger dispersion across the sample of low-mass clusters, than it does for the sample of high-mass clusters. We interpret this finding as the result of the mixing of more haloes in large clusters than in small clusters, which leads to an averaging of the metal content in the large clusters, and thus less dispersion of metallicity for high-mass clusters. This interpretation lends support to the idea that the low-entropy, metal-rich gas of merging haloes reaches clusters' centers, which explains observations of Core-Collapse Supernova products metallicity peaks, and which is seen in hydrodynamical simulations. The gas in these merging haloes would have to reach the centers of clusters without mixing in the outer regions, in order to support our interpretation. On the other hand, metallicity dispersion does not change with mass in the outer regions of clusters, suggesting that most of the outer metals come from a source with a more uniform metallicity level, such as during pre-enrichment. We also measure a correlation between the metal content in low-mass clusters and the degree to which their Intra-Cluster Medium (ICM) is morphologically disturbed, as measured by centroid shift. This suggests an alternative interpretation of the large width of the metallicity distribution in low-mass clusters, whereby a metallicity boost in the center of low-mass clusters is induced as a transitional state, during mergers.

Subject headings: galaxies: clusters: general, galaxies: clusters: intracluster medium, X-rays: galaxies: clusters

1. INTRODUCTION

In today's Universe, galaxy clusters are the largest bound structures, ranging in mass from about 10^{13} to $10^{15}M_{\odot}$. Their formation is understood within the paradigm of hierarchical structure formation, where large structures form through the merger of smaller structures. Because of their large masses, the Intra-Cluster Medium (ICM) in galaxy clusters is heated and compressed, such that bremsstrahlung emission becomes an efficient radiation process. This X-ray emission from the ICM contains within it ample information about the chemistry and the dynamical state of the ICM, and by extension the cluster as a whole. In particular we focus in this study on two quantities, metallicity and entropy, because they encode the integrated effect of various physical processes occurring in clusters.

Most metals have been produced in stars, predominantly through thermonuclear burning, or in processes resulting from the extreme conditions in supernovae (SNe). Therefore, studying metallicity in galaxy clusters probes processes that produce metals, such as star formation and SN rates, as well as processes that mix and distribute metals such as mergers and central AGN activity.

Renzini et al. (1993) were the first to point out that one cannot account for all the observed metals in the ICM assuming the current SN Type Ia rate per unit luminosity was the same in the past. This problem was studied with better SN data and more complex chemical evolution and ICM enrichment models by Portinari et al. (2004) and Loewenstein (2006), who both showed the need for more metal production in clusters, compared to what is observed in the field. Both studies above in addition to Nagashima et al. (2005), suggest that a different stellar Initial Mass Function (IMF) must operate in field galaxies than in clusters. For example, a top-heavy IMF might be necessary in galaxy clusters.

Hydrodynamical models predicting the metallicity of the ICM have been reviewed by Borgani et al. (2008). The results of these studies in terms of the effect of different IMF's on the level of enrichment vary, as some are able to match or even exceed the observed metallicity in clusters, while others cannot match it, depending on the many details and parameters of the models.

Two classes of SNe are responsible for producing the metals in clusters. Core Collapse SNe (SNCC) result from massive stars, whose lives are short compared to the time since the peak of star formation, at a redshift $z \sim 2-3$. Type Ia SNe (SNIa) result from low-mass stars and thus can be delayed by billions of years from the time of star formation. If the above picture of a prompt metal injection from SNCC, followed by a more gradual injection from SNIa holds, then we should expect this to affect the metallicity radial profiles. Each class of SNe produces a different set of elements (e.g. Werner et al. 2008). Both SN classes produce iron, while, for example, SNCC are the main contributors of oxygen, neon and magne-

---

[1] Department of Physics, Massachusetts Institute of Technology, 77 Massachusetts Avenue, Cambridge, Massachusetts 02139, USA; tykholy@gmail.com
[2] MIT Kavli Institute for Astrophysics and Space Research, 77 Massachusetts Avenue, Cambridge, Massachusetts 02139, USA

sium. Since the rate of SNCC at any epoch is roughly proportional to the then-current rate of star formation, and since clusters form relatively late, we expect SNCC products to have enriched the proto-ICM before cluster collapse. The SNCC products are therefore expected to be homogeneously spread through the ICM. Conversely, SNIa products are expected to be nearer the center of the cluster, as the Brightest Cluster Galaxy (BCG) accumulates more and more stars with time. However, using very deep *Chandra* observations, Sanders & Fabian (2006), Simionescu et al. (2009a), Simionescu et al. (2010) and Million et al. (2011) measure a large amount of SNCC products in the core of nearby galaxy clusters, presenting a challenge to the above picture.

Because entropy remains unchanged under adiabatic processes, it measures any heat input or output to the gas. In the case of the ICM, the main process that changes its entropy is gravitational shock heating. Other processes affecting the ICM entropy include radiative cooling, heating by AGN and SNe, as well as processes such as turbulent dissipation and conduction. The reader is referred to McNamara & Nulsen (2007) for a detailed review of the above processes.

Gravity is expected to be the dominant force in cluster formation, and thus most of the entropy generation is expected to result from shock heating of infalling gas, as a cluster forms. This process converts gravitational potential energy into heat. Because $S \propto T/n^{2/3}$, we expect the characteristic entropy scale of a cluster to scale proportionally to its virial temperature, or as $M^{2/3}$, where M is the cluster mass. Hydrodynamical simulations (e.g. Voit et al. 2005; Nagai et al. 2007) produce a normalization of the entropy expected from gravity, as well as a radial profile, which is proportional to a power-law of radius, $r^{1.1-1.2}$. Observationally, Ponman et al. (1999) were among the first to measure the departure of the entropy from the expected self-similar scaling with cluster mass. The same result was later found in Lloyd-Davies et al. (2000), Ponman et al. (2003), and Pratt et al. (2010).

Some studies have focused on cases where the effects of both heating and metal enrichment can be detected. High-resolution observations of the centers of clusters find regions of enhanced metallicity expected to have been ejected from the central regions of clusters, by the central engine (e.g. Simionescu et al. 2009a,b; Kirkpatrick et al. 2009; O'Sullivan et al. 2011). For example, Kirkpatrick et al. (2011) showed that the direction of elongation of an enhanced-metallicity region is correlated with the direction of cavities and radio emission axes, originating from the center. On larger scales, however, simulations by Borgani et al. (2005) and Short et al. (2013) suggest that winds from SNe have little effect on the overall entropy of clusters. There is, however, a shortage of attempts to test these results observationally.

The aim of this work is therefore to apply a systematic, spatially resolved study of metallicity and entropy to a large sample of galaxy clusters, to look for any possible relation between the metallicity and the entropy of the ICM. We also aim to produce a dataset of entropy profiles (in the form of temperature and metallicity profiles) for the community to employ in various galaxy cluster studies, and make it available electronically.

Throughout this work a ΛCDM cosmological model is assumed, where the Hubble constant is $H_0 = 72$ km/s/Mpc, the matter density parameter $\Omega_m = 0.26$, the dark energy density is $\Omega_\Lambda = 0.74$, and the universal baryon fraction, $f_b = \Omega_b/\Omega_m = 0.169$, where Ω_b is the baryon density.

2. DATA SAMPLE AND ANALYSIS

2.1. *Data Sample*

Our sample consists of bright clusters — present in both the HIFLUGCS and ACCEPT samples — which were observed with *Chandra*'s ACIS instrument out to at least $0.2R_{500}$, where R_{500} is the radius enclosing an average density that is 500 times the critical density of the Universe at the redshift of the observed cluster. More precisely, we start with the extended HIFLUGCS sample of galaxy clusters, which is a flux-limited sample of clusters with X-ray flux $f_X[0.1 - 2.4keV] \geq 2 \times 10^{-11}$ erg/s/cm^2 (Reiprich & Böhringer 2002). We search for the HIFLUGCS clusters which have *Chandra* coverage[3] out to at least $0.2R_{500}$. Once the above sample is identified, we search the ACCEPT data for the aforementioned HIFLUGCS subsample, where entropy is measured in at least 3 radial bins beyond $0.2R_{500}$. The ACCEPT study (Cavagnolo et al. 2009) measured the entropy profiles of all galaxy clusters observed by *Chandra*, up to August 2008, and has made the data available online[4]. Forty eight galaxy clusters satisfy the above selection criteria.

For all spectral analysis, we discard all observations taken before January 29, 2000 as the *Chandra* focal plane temperature for that period was −110°C or higher, which increases the level of background. *Chandra*'s calibration is in general better for later dates. Only one cluster, Abell 401, is excluded from our analysis because it was only observed prior to January 29, 2000. We also exclude Abell 2255 because its available observation was too short to yield enough photons. The complete analysis will thus be presented for a sample of 46 clusters.

We show in Table 1 the observational details of our sample, and the *Chandra* observations used in this work. For each cluster, we show the label which will be used to designate it hereafter, in figures and tables. We show the cluster's celestial coordinates, and its redshift. We list the *Chandra* Observation ID's (OBSID) we use in this work. Some OBSID's are shown in parentheses. These are the observations that were used in imaging analysis, and excluded from spectral analysis, as described above. Finally, we show the total exposure time used in the spectral analysis of each cluster.

2.2. *Data Preparation*

We use the Chandra Interactive Analysis of Observations software, more commonly known as CIAO[5], for analysis in this work. More precisely, we use CIAO's 4.2 version. Data are reprocessed following the guidelines in the CIAO analysis thread "Reprocessing Data to Create New Level=2 Event File", using the tool

---

[3] For the purpose of selecting clusters, we use the values of R_{500} measured in Reiprich & Böhringer (2002).

[4] http://www.pa.msu.edu/astro/MC2/accept/

[5] http://cxc.harvard.edu/ciao/

TABLE 1: *Chandra* Observations.

Cluster[a]	Label[b]	RA[c]	Dec[d]	z[e]	Obsids[f]	T (ks)[g]
Abell 119	a119	00:56:15.392	-01:15:17.78	0.044	4180, 7918	57
Abell 1413	a1413	11:55:17.986	+23:24:17.82	0.1427	1661, 5002, 5003	121
Abell 1644	a1644	12:57:11.772	-17:24:33.68	0.0474	2206, 7922	70
Abell 1651	a1651	12:59:22.188	-04:11:45.80	0.086	4185	10
Abell 1689	a1689	13:11:29.495	-01:20:29.02	0.184	5004, 540, 6930, 7289	181
Abell 1736	a1736	13:26:54.235	-27:09:48.65	0.0461	10428, 10429, 10430, 10431, 4186	35
Abell 1795	a1795	13:48:52.668	+26:35:30.73	0.0616	10898, 10899, 10900, 10901, 12026, 12028, 12029, 13106, 13107, 13108, 13109, 13110, 13111, 13112, 13113, 13412, 13413, 13414, 13415, 13416, 13417, 5286, 5287, 5288, 6159, 6160, 6161, 6162, 6163, (494)	437
Abell 1914	a1914	14:26:01.072	+37:49:32.97	0.1712	3593, (542)	27
Abell 2029	a2029	15:10:56.091	+05:44:40.94	0.0767	10437, 4977, 6101, 891	112
Abell 2063	a2063	15:23:05.323	+08:36:28.49	0.0354	5795, 6263	27
Abell 2065	a2065	15:22:29.060	+27:42:34.33	0.0721	3182	22
Abell 2142	a2142	15:58:20.103	+27:13:58.76	0.0899	5005, (1196, 1228)	68
Abell 2147	a2147	16:02:15.608	+15:57:53.77	0.0351	3211	18
Abell 2163	a2163	16:15:46.519	-06:08:50.57	0.201	1653, 2455, 545	89
Abell 2204	a2204	16:32:46.922	+05:34:31.40	0.1523	499, 6104, 7940	97
Abell 2244	a2244	17:02:42.517	+34:03:37.46	0.097	4179	57
Abell 2256	a2256	17:03:59.388	+78:38:44.57	0.0601	2419, (1386, 965)	35
Abell 2319	a2319	19:21:09.997	+43:57:18.82	0.0564	3231	14
Abell 2657	a2657	23:44:56.531	+09:11:28.75	0.0404	4941	16
Abell 2734	a2734	00:11:21.616	-28:51:17.98	0.062	5797	20
Abell 3112	a3112	03:17:57.627	-44:14:20.34	0.075	2216, 2516, 6972, 7323, 7324	108
Abell 3158	a3158	03:42:52.591	-53:37:50.03	0.059	3201, 3712	56
Abell 3376	a3376	06:01:57.312	-39:58:25.80	0.0455	3202, 3450	64
Abell 3391	a3391	06:26:20.780	-53:41:32.98	0.0531	4943	18
Abell 3571	a3571	13:47:28.580	-32:51:14.35	0.0397	4203	34
Abell 3667	a3667	20:12:36.316	-56:50:40.74	0.056	5751, 5752, 6292, 6295, 6296, 889, (513)	430
Abell 3822	a3822	21:54:06.292	-57:51:41.06	0.076	8269	8
Abell 3827	a3827	22:01:53.279	-59:56:45.99	0.098	7920	46
Abell 3921	a3921	22:49:57.845	-64:25:44.13	0.0936	4973	29
Abell 399	a399	02:57:51.557	+13:02:32.43	0.0715	3230	49
Abell 400	a400	02:57:41.119	+06:01:20.03	0.024	4181	21
Abell 4038	a4038	23:47:43.200	-28:08:38.30	0.0283	4188, 4992	40
Abell 4059	a4059	23:57:00.933	-34:45:34.44	0.046	5785, 897	110
Abell 478	a478	04:13:25.199	+10:27:53.90	0.09	1669, 6102	52
Abell 539	a539	05:16:36.680	+06:26:34.63	0.0288	5808, 7209	43
Abell 644	a644	08:17:25.392	-07:30:48.38	0.0704	10420, 10421, 10422, 10423, 2211	49
Abell 754	a754	09:09:21.084	-09:41:05.78	0.0528	10743, 6793, 6794, 6796, 6797, 6799, (577)	187
Abell S 405	as405	03:51:29.787	-82:13:21.26	0.0613	8272	8
Hydra A	hyda	09:18:05.876	-12:05:43.17	0.0538	4969, 4970, (575, 576)	239
Zw III 54	iiizw54	03:41:17.508	+15:23:54.82	0.0311	4182	23
MKW 3S	mkw3s	15:21:51.708	+07:42:24.65	0.045	900	57
MKW 8	mkw8	14:40:39.353	+03:28:03.08	0.027	4942	23
PKS 0745-191	pks0745-191	07:47:31.265	-19:17:41.62	0.1028	2427, 508, 6103	56
UGC 3957	ugc3957	07:40:58.133	+55:25:38.25	0.034	8265	8
ZwCl 1215+0400	z1215	12:17:41.934	+03:39:39.74	0.075	4184	12
ZwCl 1742+3306	z1742	17:44:14.447	+32:59:29.02	0.0757	11708, 8267	53

[a] Cluster name.

[b] Label used to denote cluster.

[c] Cluster right ascention.

[d] Cluster declination.

[e] Cluster redshift.

[f] The *Chandra* OBSID's used in this work. OBSID's in parantheses were used in imaging analysis, and excluded from spectral analysis.

[g] The total exposure time for spectral analysis in kiloseconds.

`acis_process_events`. This reprocessing includes filtering to keep only event grades 0, 2, 3, 4 and 6. In addition, the VFAINT background cleaning method is applied to observations in VFAINT mode, using the `check_vf_pha=yes` option to `acis_process_events`.

The center of the clusters is defined to be the centroid of event x- and y-coordinates, calculated using the following iterative scheme. First, we select the observation with the longest exposure time, in the cases where we have multiple observations of one cluster. For ACIS-I pointing, we calculate the centroid using all four ACIS-I chips, while for ACIS-S pointings, we only use the chip with the most counts. We only include events with energies between 0.3 and 7keV. For the first centroid computation iteration, Iteration 1, we calculate the medians and the standard deviations of the x- and y-coordinates of the events from the entirety of the selected chip(s) of the longest-exposure observation. For Iteration 2, we restrict the median and standard deviation calculation to events within an ellipse with semi-major axes equal to *twice* the x and y standard deviations calculated in Iteration 1, i.e. $2 \times (\sigma_{x1}, \sigma_{y1})$. For Iteration 3, the ellipse is shrunk to have semi-major axes equal to $1 \times (\sigma_{x2}, \sigma_{y2})$. Similarly, Iteration 4's filter ellipse has semi-major axes $0.75 \times (\sigma_{x3}, \sigma_{y3})$. For the final iteration, Iteration 5, we employ events from all observations in the centroid computation, instead of using the longest-exposure observation alone. The Iteration 5 filter ellipse has semi-major axes equal to $1 \times (\sigma_{x4}, \sigma_{y4})$.

Events from point sources are then identified and discarded. We use CIAO's `wavdetect` tool, applied to an image of the merged event files from all observations. The input image to `wavdetect` includes only events with energies in the range 0.3-7keV and is binned in (2×2)-pixel bins. The detected point source regions are inspected by eye to ensure that each region is large enough to include all events from its corresponding detected point source, and to add sources that were not detected by `wavdetect`. The latter tend to be point sources away from the telescope's optical axis, where the point spread function is much larger than it is in the center. We also exclude any region of bright extended emission, which does not belong to the central cluster emission, such as that from infalling sub-clusters (e.g. the sub-cluster to the North of Abell 2163.) We expect that many clusters will contain emission from faint infalling sub-clusters, which cannot be resolved due to their low surface brightness. Therefore we do not attempt to discard all emission from identified sub-clusters, and only remove the bright peaks of such emission when present.

Periods of high count rates resulting from flares are removed using the `lc_clean()` tool in *Sherpa*, which is CIAO's tool for spectral analysis. We compute a light curve of all data counts, excluding the point sources detected above, and the central 300" to exclude the bulk of the cluster emission. Short flares are excluded when they are identified by `lc_clean()`, while longer flares are excluded manually by selecting events in the time range which is sufficiently removed from the the start or the end of the flare. Some observations in which one or many flares last for most of the exposure time are entirely excluded.

For each observation, we create a background dataset from the Blank Sky files, available as part of the *Chandra* calibration files. We choose the Blank Sky file for each ACIS chip based on the cluster dataset's observation date, its aim point and whether a CTI correction was applied to it. As mentioned above, we exclude all data taken prior to January 29, 2000. No Blank-Sky datasets are available in Period C, in VFAINT mode. We therefore assign to these datasets, the Blank-Sky files from Period D in VFAINT mode. In addition, we exclude some ACIS-S data taken during Period C, because their corresponding Blank-Sky files are not available[6].

2.3. *Data Analysis*

As is custom in clusters astrophysics, we define entropy as $S = kT/n_e^{2/3}$, where k is Boltzmann's constant, T the ICM temperature, and n_e its electron density. As defined above, S is related to the thermodynamical entropy per particle, s, through $s = (3k/2)\ln S + s_0$, where s_0 only depends on fundamental constants. We assume spherical symmetry and compute the entropy radial profiles from the density and temperature profiles, as described below.

2.3.1. *Density Profile, $n_e(r)$*

Computing the electron density profile of the ICM is done in two steps. First, we use surface brightness (SB) measurements to constrain the shape of the density radial profile. Then, we use spectral measurements to set the overall normalization of $n_e(r)$. To fit for the density profile shape, we extract a SB profile based on photon counts in the energy range 0.7–2keV. Radial bins are defined such that boundary radii are spaced logarithmically, with a constant ratio of 1.25 between neighboring radii, except when this spacing results in fewer than 100 counts in the bin, in which case it is extended to the next radius. The innermost radius is defined as the projection of 1.2 arcseconds in the plane of the cluster, in order to include the largest number of counts, while avoiding any potential point source coinciding with the centroid of the ICM X-ray emission. From the source counts in each radial bin, we subtract the background contribution computed from the blank-sky datasets, and scaled by detector area and exposure time to match each observation and radial bin. The net number of counts is then normalized by the exposure map, to correct for the position dependence of *Chandra*'s effective area. Finally we obtain a count SB by dividing by the solid angle of the extraction region.

The emissivity of an X-ray plasma at cluster temperatures is primarily in the form of bremsstrahlung and line emission. The contribution of each of those processes is proportional to n_e^2, but depends differently on the plasma temperature. However, when emissivity is integrated over the 0.7–2keV energy range, the different temperature dependencies contrive to cancel each other, and the resulting emission in this energy band has a negligible temperature dependence. In addition, we assume the ICM to be optically thin. Therefore, the SB at any given point on the sky is simply the integral of all emission along the line of sight to that point. We perform a maximum-likelihood fit to find the density profile that best fits the counts SB profile, up to a normalization. We use an analytical form for $n_e(r)$ that is flexible enough to allow us to phenomenologically fit the SB in all radial bins. Namely, we choose a simplified version of Vikhlinin's extended beta model (Vikhlinin et al. 2006),

---

[6] The definition of the background periods used here is available in Maxim Markevitch's note at http://cxc.harvard.edu/contrib/maxim/acisbg/COOKBOOK

$$\frac{n_e^2(r)}{n_0^2} = \frac{(\frac{r}{r_c})^{-\alpha}}{(1+\frac{r^2}{r_c^2})^{3\beta-\alpha/2}} \frac{1}{(1+(\frac{r}{r_s})^3)^{\epsilon/3}} , \quad (1)$$

where n_0, r_c, β, α, r_s and ϵ are fit parameters. In each iteration of the fitting process, and for a given radial bin bound by radii r_i and r_{i+1}, we integrate $n_e^2(r)$ over the volume of the cylindrical shell defined by the above two radii and extending along the line of sight from -3Mpc to $+3$Mpc. The set of integrals from all radial bins is then compared to the corresponding SB values to determine the shape parameters in the right hand side of Equation 1.

This procedure provides the shape but not the normalization, n_0, of the density profiles. Computing n_0 requires knowledge of the emission integral measure, $EI = \int n_e n_p dV$, where n_p is the proton number density. This integral quantity, EI, is simply proportional to the normalization of the APEC spectral model, which we use to model ICM emission. The APEC model (Smith et al. 2001) is fit to the spectra of multiple radial bins around the center of emission. The normalization of the spectral model of the i^{th} radial bin, K_i, is related to EI_i through

$$K_i = \frac{0.82\ 10^{-14}}{4\pi D_A^2(1+z)^2}\ n_0^2 V_i \ , \quad (2)$$

where z is the cluster redshift and D_A its angular diameter distance. We define V_i as the spatial integral of $(n/n_0)^2$ over the cylinder defined by the i^{th} radial bin and bounded along the line of sight direction by $\ell = \pm 20$Mpc. We have assumed above that $n_e = 0.82 n_p$, which is suitable for typical ICM conditions. The best-fit n_0 is determined by minimizing

$$\chi^2_{n_0} = \sum_i \frac{\left(K_i - C_D V_i n_0^2\right)^2}{\delta K_i^2} \quad (3)$$

with respect to n_0^2, where δK_i is the uncertainty on K_i and $C_D \equiv 0.82\ 10^{-14}/4\pi D_A^2(1+z)^2$.

2.3.2. *Temperature Profile, $kT(r)$*

To compute the temperature profiles, we again construct radial bins, and fit their spectra, resulting in a projected temperature profile. We then deproject the above temperature profile, using similar methods to those used to deproject the density profile. We choose the size of the radial bins in order to include the lowest number of counts necessary for a temperature determination, with 10% uncertainty. This count number, N_{nec}, which is a function of temperature and background count fraction, is estimated by simulating spectra of different total counts, temperatures and background fractions, f_{bg}, to find the necessary counts for a 10% uncertainty on temperature (Elkholy 2012). We find that N_{nec} can approximately be fit by

$$N_{nec}(kT, f_{bg}) = 500 \times 10^{1.976 f_{bg}} \times \left(\frac{kT}{2\mathrm{keV}}\right)^{1.7} . \quad (4)$$

We extract spectra of at least N_{nec} counts and fit their spectra to an absorbed APEC model in CIAO's tool, *Sherpa*. We create a spectrum from each observation that partially or wholly covers the annulus corresponding to a radial bin, and simultaneously fit these spectra. We link the temperatures and metal abundances of these spectra, across the multiple observations, during the fit. Normalizations are only linked for spectra that cover more than 95% of the solid angle of the annular region. Metallicity is left as a free parameter, while the hydrogen column density, n_H, is fixed to the values from the LAB dataset of Kalberla et al. (2005). We also include in our online dataset the results of analysis with Dickey & Lockman (1990) n_H measurements. We find that leaving n_H as a free parameter returns unreasonable best-fit values on both n_H and temperature. However, for Abell 478, which is reported to have varying n_H by Vikhlinin et al. (2005), we allow n_H to be free, with a minimum equal to the 21-cm-measured value.

The background spectrum is extracted from the *Chandra* blank sky datasets and from source free regions around cluster observations. The background is modeled as particle background, plus X-ray background. The X-ray background is modeled as an absorbed 0.2keV APEC model, with $n_H = 2.09 \times 10^{22}$ cm^{-2} and an absorbed power-law component for the Cosmic X-ray Background, with index set to -1.4. These components are convolved with the instrument response for each CCD chip. The particle background is modeled as a series of Gaussian, exponential, and a power-law functions, to phenomenologically fit the remaining components of the blank sky datasets. It is not convolved with the instrument response. The overall background spectral model varies from epoch to epoch, and also depends on the CCD chip used.

We assume that the shape of the instrumental background component of the cluster observation is the same as the best-fit model from the corresponding blank sky dataset and compute its normalization as suggested in Maxim Markevitch's cookbook for treating the background data[7]. The overall normalization of the instrumental background is computed by scaling the background normalization according to the ratio of counts in the 9.5-12 keV energy range, in the cluster dataset relative to the blank sky dataset. In this manner we attempt to capture any possible change in the background normalization between different epochs. We note that datasets in our sample with OBSID between 7686 and 7701 are missing high-energy counts. Their instrumental background normalization is thus scaled simply by exposure time and solid angle.

Having used the blank sky data to constrain the instrumental background components, we proceed to fit the X-ray background from the in-field spectra. The latter are modeled with the same model described above plus an additional APEC component to account for residual cluster emission. The APEC model's temperature is fixed at the temperature measured outside a projected radius of 150kpc, using an initial simple fit.

---

[7] http://cxc.harvard.edu/contrib/maxim/acisbg/COOKBOOK

The in-field spectra are obtained from annuli centered around the cluster center, and covering regions that are visually identified to contain mostly background X-ray counts. For Abell 119 and Abell 3571, the cluster emission covers most of the field of view (FOV.) We thus rely on the blank sky background data to model both instrumental and X-ray background components, for these two clusters.

We use CSTAT as our fit statistic, as it is more suitable for energy bins with low counts, where the more commonly used χ^2 statistic introduces bias. After obtaining the best-fit temperature, we compute its uncertainty using *Sherpa*'s `proj()` function, which varies temperature along a grid and searches for the best-fit at each temperature by varying the other thawed parameters.

The spectral fitting described above, returns a best-fit *projected* temperature for a given radial bin: Since the ICM is thought to be optically thin, the emission at one point on the sky is the sum of all emission from the line of sight behind that point. Thus, to compute the true three-dimensional temperature profile, we assume a flexible analytic form for $kT(r)$, vary its parameters repeatedly, projecting it along the line of sight in each iteration until the best match is found with the measured projected temperature radial profile. This fitting process is again run using *Sherpa*. The projection is computed according to the prescription in Mazzotta et al. (2004), who show that to recover a single-temperature fit from a mixture of many temperature components, one should average these temperatures with a weighting proportional to n^2VT^α, where V is the volume of the region of emission. We choose $\alpha = -0.75$, as suggested by the range of values found by Mazzotta et al. (2004) for spectra of different metallicities. The three-dimensional temperature profile is modeled as in Vikhlinin et al. (2006):

$$kT(r) = kT_0 \; \frac{(r/r_t)^{-a}}{[1+(r/r_t)^b]^{c/b}} \; \frac{x + T_{min}/T_0}{x+1} \; , \qquad (5)$$

where $x = (r/r_{cool})^{a_{cool}}$ and where T_0, r_t, a, b, c, T_{min}, r_{cool} and a_{cool} are fit parameters. The number of free parameters depends on the number of available temperature measurements.

Computing $kT(r)$ and $n_e(r)$ gives us the necessary quantities to measure R_{500}, the gas mass within R_{500}, which we call M_{gas}, and the total gravitational mass within the same radius, M_{500}. As described in Elkholy (2012), we do so using an iterative scheme, since the 3 quantities are related. We use the $M - Y_X$ relation of Kravtsov et al. (2006) to relate M_{500} to our measurables, as $Y_X \equiv kT_X M_{gas}$.

2.3.3. *Uncertainties*

The uncertainties on the entropy profile of each cluster are estimated by generating a set of $S(r)$ models, which are allowed by the data and their uncertainties, as descibed here. For temperature radial profiles, using the temperature measurements in each radial bin, and their error estimate, we randomly generate new “fake” datasets, and fit them one at a time. To generate a fake temperature measurement for each radial bin, we draw its value from a random distribution designed to capture the asymmetric uncertainties obtained on the bin's best-fit temperature. This probability distribution is a piecewise function of 2 Gaussian distributions on either side of the best-fit temperature, with the standard deviations equal to the measured 1-σ upper and lower uncertainties. The latter are not in general equal to each other. Once a complete radial temperature profile is generated over the entire available radial range, we fit it with the same model in Equations 5, and repeat this analysis for 400 iterations.

The same analysis is repeated for the density profiles, where surface brightness measurements are similarly perturbed for 300 iterations according to their uncertainties. The uncertainties in this case are assumed to be symmetric, and the fake surface brightness measurements are drawn from a Gaussian distribution.

To compute the uncertainty on the entropy profile, we compute a set of entropy profiles from pairing different temperature and density profiles, from the above generated sets. We iterate through all 400 temperature profiles. For each temperature profile, we iterate through 10 density profiles computing a temperature profile $S(r) = kT(r)/n_e(r)^{2/3}$, in each iteration. We ensure to choose different density profiles, from one temperature profile to the next, until all 300 profiles are used, at which point we start from the beginning of the density profiles list. The result is an ensemble of 4000 entropy profiles, which we use to find the distribution of entropy values at any given radius.

2.3.4. *Metallicity Profile Calculation Method*

To compute the metallicity profiles, we take a similar approach to that used to make the temperature profiles. First, using simulated spectra, we estimate the minimum necessary counts, $N^Z_{nec}(kT, Z, f_{bg})$, to obtain a 20% uncertainty on the best-fit metallicity. In this case, $N^Z_{nec}(kT, Z, f_{bg})$ does not have a simple analytical form as its counterpart for temperature measurement, but is rather estimated from a weighted average of N^Z_{nec} values estimated for the kT, Z and f_{bg} values that were simulated (Elkholy 2012). Then, using the derived N^Z_{nec}, we extract spectra in radial bins using the same bins used fo the $kT(r)$ profile calculation, and joining them whenever more counts are needed for a 20%-uncertainty temperature estimate. We take the maximum radius of extraction to be R_{500}.

For spectral fitting, we again model both source emission from the ICM and background. For the background spectra, we use the same best-fit parameters found in the $kT(r)$ analysis, above. The background normalization is computed using the same method as in the $kT(r)$ analysis, described in Section 2.3.2. Cluster emission is modeled using a 1-temperature model, and using a 2-temperature model, where the cooler component's temperature is set to one half of the value of the hotter component's temperature.

We compute the uncertainty on the metallicity in each bin using *Sherpa*'s `proj()` function. From the obtained metallicity profile, we characterize the metallicity of each cluster by two global quantities, $\bar{Z}_{mid}$ and $\bar{Z}_{in}$. We define

$$\bar{Z}_{mid} = \frac{\sum_{0.15<r_i<0.3R_{500}} Z_i M_{gas,i}}{\sum_{0.15<r_i<0.3R_{500}} M_{gas,i}} \; , \qquad (6)$$

which is the gas-mass-weighted metallicity over all shells in the range $0.15 < r < 0.3R_{500}$. Here, Z_i and $M_{gas,i}$ are, respectively, the metallicity and the gas mass in the i^{th} radial bin. In other words, $\bar{Z}_{mid}$ traces the total iron mass, M_{Fe}^{mid}, in the region $0.15R_{500} < r < 0.3R_{500}$, according to

$$M_{Fe}^{mid} = A_{Fe}\bar{Z}_{mid}M_{gas}^{mid} \ , \tag{7}$$

where $A_{Fe} = 0.0019$ is the solar abundance of iron by mass, according to the photospheric measurements in Anders & Grevesse (1989) assumed for our spectral analysis, and M_{gas}^{mid} is the gas mass contained in the same region. Similarly,

$$\bar{Z}_{in} = \frac{\sum_{r_i<0.15R_{500}} Z_i M_{gas,i}}{\sum_{r_i<0.15R_{500}} M_{gas,i}} \ . \tag{8}$$

Hereafter, $\bar{Z}_{mid}$ will be used as a measure of the metallicity of the bulk of a cluster, while $\bar{Z}_{in}$ will be used as a measure of the core metallicity in clusters.

3. RESULTS

We make our data available on the FTP site[8]

`ftp://space.mit.edu/pub/tamer/ebc2015/` .

Appendix A contains the plot of the entropy profile for each cluster, while the individual metallicity radial profiles are shown in Appendix B.

We first note that 4 clusters of our sample deviate considerably from spherical symmetry simply based on their surface brightness image. These clusters, Abell 754, Abell 2256, Abell 3376 and Abell 3667, are known to be undergoing merging events. We exclude the disturbed clusters from our analysis, except when noted.

Table C1 in Appendix C shows the measured values of kT_X, R_{500}, M_{500} and M_{gas} for each cluster.

3.1. *Entropy Profiles*

Our best-fit results for density and temperature radial profiles are shown in Tables D1 and D2, respectively, in Appendix D.

We overplot the computed entropy profiles for all of our sample's clusters in Figure 1. On the left panel, we plot entropy as a function of radius, which we normalize with respect to R_{500}. On the right panel, we plot entropy as a function of enclosed gas mass fraction, $F_g \equiv M_g/(f_b M_{500})$, where M_g is the interior gas mass, and f_b the universal baryon fraction with respect to all matter, i.e. $f_b = \Omega_b/\Omega_m$. We use F_g to plot entropy profiles because this is the variable used in a Lagrangian description of the entropy distribution in clusters (see e.g. Tozzi & Norman 2001; Voit et al. 2003; Nath & Majumdar 2011). The entropy in both panels is normalized with respect to S_{500} (Voit et al. 2003), the characteristic entropy of the cluster at R_{500}:

$$S_{500} \equiv \frac{GM_{500}\mu m_p}{2R_{500}\left[500 f_b \rho_c(z)/\mu_e m_p\right]^{2/3}} \ , \tag{9}$$

where μ and μ_e are the mean number of nucleons per particle and per electron, respectively, m_p is the proton mass and $\rho_c(z)$ is the Universe's critical density at the redshift of observation, z. The characteristic entropy, S_{500} at an overdensity $\delta = 500$ is simply the entropy obtained using the characteristic temperature at $\delta = 500$, which is the equivalent of the virial temperature but defined for R_{500} instead of the virial radius,

$$kT_{500} \equiv \frac{GM_{500}\mu m_p}{2R_{500}} \ , \tag{10}$$

and using the average electron density inside R_{500},

$$\bar{n}_e = 500 f_b \rho_c(z)/\mu_e m_p \ . \tag{11}$$

It represents the entropy scale set by gravity in the self-similar picture.

The dark blue line in Figure 1 represents a model of the entropy profile of a cluster generated from gravitational collapse alone, which was calculated with hydrodynamical AMR simulations in Voit et al. (2005). Voit's entropy profile is approximated analytically as a power law,

$$S_V(r) = 1.53 S_{500}\left(\frac{r}{R_{500}}\right)^{1.24} \ , \tag{12}$$

and is valid for radii larger than approximately $0.2R_{500}$. We employ the conversion used in Pointecouteau et al. (2005) to express Equation 12 in terms of S_{500} and R_{500}, as opposed to the measurements at an overdensity of 200, presented in Voit et al. (2005).

Turquoise curves in Figure 1 represent cool core clusters (CC), while red curves are for non-cool core clusters (NCC). We use the surface brightness concentration, c_{SB}, introduced in Santos et al. (2008) to quantify the cool core state of a cluster. The parameter c_{SB} is defined as the ratio of the surface brightness within 40 kpc to that within 400kpc of the *peak* of the emission[9]. The values of c_{SB} are shown in Table E1. We define CC clusters as clusters with $c_{SB} > 11$, while NCC cluster have $c_{SB} < 11$.

The first observation to make is that for most of the studied radial range, all entropy profiles lie above Voit's 2005 gravitationally induced entropy model. This result has been known in the literature (e.g. Ponman et al. 1999; Pratt et al. 2010), and the additional entropy in the observations has been attributed to non-gravitational processes, such as winds and AGN heating. Second, some of the entropy profiles in Figure 1 show a decrease or a flattening starting at a radius between 0.3 and $0.8R_{500}$. This is due to a decrease in measured temperature towards the outskirts of many clusters, which is not matched by a steep enough decrease of measured density with radius. Such a configuration of large amounts of lower-entropy gas at larger radii is not physically stable. There are two sources of systematic error that can be contributing here to give erroneous temperature and density measurements. First, systematics in our estimate of the level of X-ray background will translate into an error in the estimate of the cluster surface brightness at

---

[8] The file named "README" within this FTP site details the content of the data.

[9] For calculating c_{SB}, we use the emission peak as the cluster center, unlike in previous analysis where the emission is used instead.

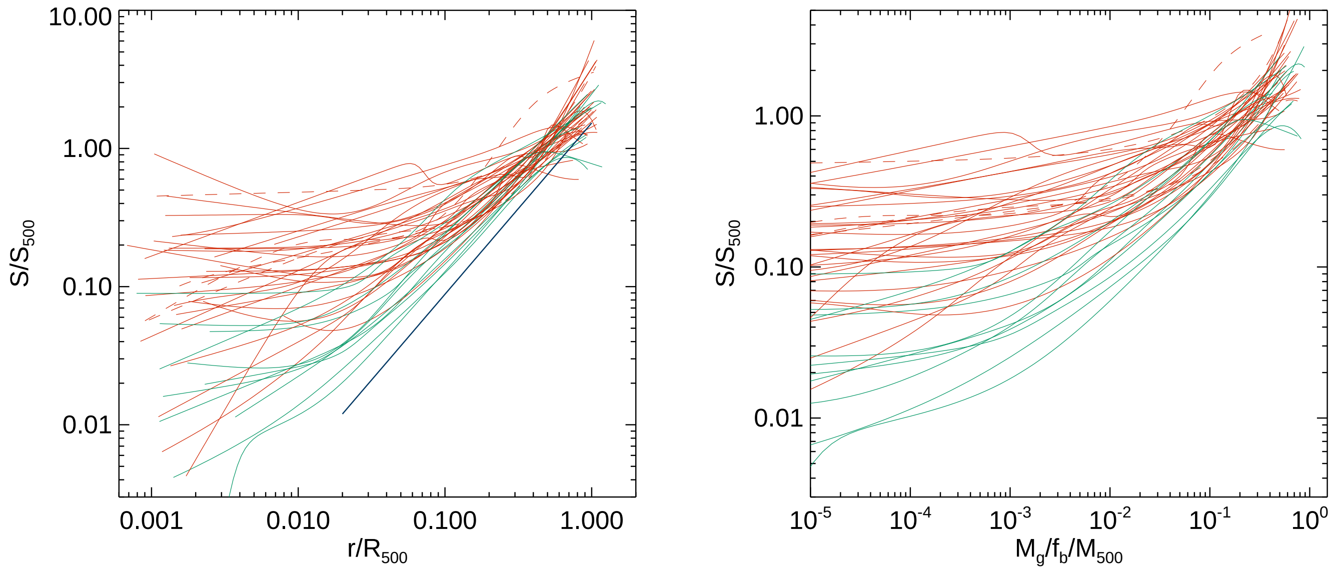

FIG. 1: Plot of all computed entropy profiles. *Left:* scaled entropy, S/S_{500}, as a function of scaled radius, r/R_{500}. *Right:* scaled entropy as a function of enclosed gas mass fraction, F_g. Turquoise curves are for CC clusters, while red curves are for NCC clusters. The dark blue curve is the power law describing the Voit 2005 entropy profile found in hydrodynamical simulations. Dashed curves are for the 4 morphologically disturbed clusters Abell 754, Abell 2256, Abell 3376 and Abell 3667.

these large radii, introducing a bias to the inferred density, and also biasing outer temperature estimates. Second, the deprojection method of Mazzotta et al. (2004), which we employ to deproject the measured 2D temperature profile to a 3D $kT(r)$, is known to be less accurate when there is significant contribution to the emission from spectral components with temperatures smaller than ~ 3keV (Mazzotta et al. 2004; Vikhlinin 2006).

In addition, we show in Figure A1, in Appendix A, the individual entropy profiles we compute. The estimate of the 1-sigma range of entropy at each radius is represented by the turquoise shaded region. The uncertainty in the measured temperatures, which translates into an uncertainty in the parameters of the temperature radial profile, is the main contributor to the uncertainty in the entropy profile. By comparison, the contribution of the density uncertainty to the entropy uncertainty is much smaller.

The light gray error bars, in Figure A1, represent the entropy profiles measured in the ACCEPT study by Cavagnolo et al. (2009). Our entropy profiles agree, in general, with the ACCEPT entropy profiles, where they overlap. However, we extend our entropy profiles to larger radii, where we model both density and temperature.

3.2. *Metallicity Profiles and Global Measurements*

3.2.1. *Profiles*

We overplot all obtained metallicity profiles in Figure 2. The dispersion in the values of observed cluster metallicities decreases for radii larger than $0.1-0.2R_{500}$, despite the larger uncertainty associated with measured metallicities at these high radii. One metallicity measurement seems to be exceptionally larger, at large radius, as seen in Figure 2. This is the last metallicity measurement for Abell 2204, where modeling the background is likely suffering from systematics, despite an acceptable fit statistic. The outermost spectra for Abell 2204 are found to have excess low-energy counts, which are mostly fit by our galactic X-ray background component.

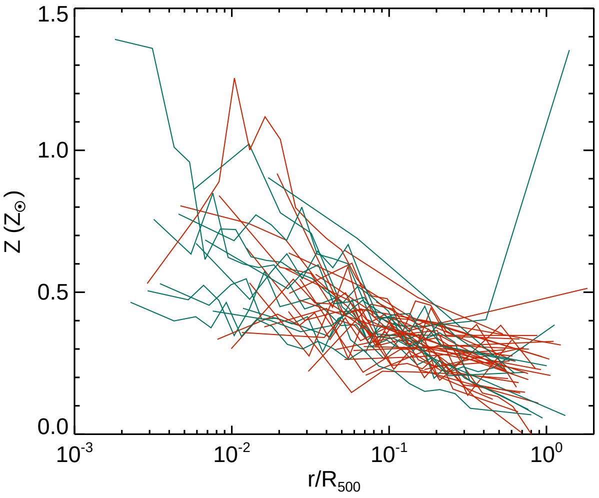

FIG. 2: Superimposed metallicity profiles of clusters. Red curves are for NCC clusters, while turquoise curves are for CC clusters.

We also present in Appendix B plots of our measured metallicity profiles, individually, with their estimated uncertainty. The two vertical lines in Figure B1 are drawn at radii $0.15R_{500}$ and R_{500}, for those clusters where we can measure M_{500} and R_{500} using our iterative method.

3.2.2. *Core Metallicity, $\bar{Z}_{in}$*

The measured values of $\bar{Z}_{in}$ are shown in Table F1, in Appendix F. We plot $\bar{Z}_{in}$ as a function of cluster mass, and as a function of the global temperature measurement, kT_X, in Figure 3. Figure 3 suggests that low-mass clusters ($M_{500} < 3.5 \times 10^{14} M_\odot$) exhibit more dispersion in $\bar{Z}_{in}$ than high-mass clusters do.

To quantify this latter observation, we show in Table 2 the error-weighted mean, and the standard deviation of the values of $\bar{Z}_{in}$, for clusters grouped by mass. The results for the 1-temperature fit are labeled "1T", and those for the 2-temperature fit "2T." The standard deviation of $\bar{Z}_{in}$ for clusters with $M_{500} > 3.5 \times 10^{14} M_\odot$ is 2.4 to 2.9 times smaller than that for clusters with $M_{500} < 3.5 \times 10^{14} M_\odot$, for the 1T and the 2T models, respectively. The value of χ^2 for each subset shows whether the dispersion for low-mass clusters is solely the result of measurement uncertainties. Here,

$$\chi^2 = \sum_i \frac{\left(\bar{Z}_{in,i} - \langle \bar{Z}_{in} \rangle\right)^2}{\delta \bar{Z}_{in,i}^2} \ , \tag{13}$$

where the sum is over the sample of clusters denoted by i, $\bar{Z}_{in,i}$ is the i^{th} cluster's central metallicity, $\delta \bar{Z}_{in,i}$ is its uncertainty and $\langle \bar{Z}_{in} \rangle$ the sample mean.

For low-mass clusters, we find that χ^2 is more than 30 times the number of degrees of freedom, for both 1T and 2T fits. This confirms that the dispersion seen in low-mass clusters — in the range $(0.12 - 0.15) Z_\odot$ — is not driven by measurement uncertainties. On the contrary, the dispersion of $\bar{Z}_{in}$ in high-mass clusters has a more significant contribution from measurement uncertainties, despite being much smaller at $\sim 0.05 Z_\odot$.

TABLE 2: Statistics for $\bar{Z}_{in}$.

	Model	Mean ($Z_\odot$)	Std. Dev. ($Z_\odot$)	χ^2/dof
$M_{500} < 3.5 \times 10^{14} M_\odot$	1T	0.30	0.12	33. (490./15)
	2T	0.25	0.15	31. (470./15)
$M_{500} > 3.5 \times 10^{14} M_\odot$	1T	0.36	0.050	2.6 (64./25)
	2T	0.35	0.052	1.2 (29./25)

Note. — Error-weighted mean, standard deviation of $\bar{Z}_{in}$ and χ^2/dof with respect to calculated mean. Results shown for clusters with M_{500} smaller than and larger than $3.5 \times 10^{14} M_\odot$, and for fits using the 1T and the 2T spectral models

The above results are unchanged when we include the $\bar{Z}_{in}$ measurements from the high-mass, asymmetrical clusters Abell 754, Abell 2256 and Abell 3667, which have $\bar{Z}_{in} = 0.369^{+0.036}_{-0.035}$, $0.389^{+0.065}_{-0.061}$ and $0.345^{+0.012}_{-0.011} Z_\odot$, respectively. These clusters were excluded from the above analysis based on their asymmetric morphologies. The 1T dispersion of $\bar{Z}_{in}$, over the high-mass subset decreases to $0.047 Z_\odot$, when the above 3 clusters are included, while the 2T dispersion does not change significantly.

To emphasize the difference between low- and high-mass clusters metallicity dispersions, we show in Figure 4 the superimposed metallicity radial profiles of all clusters in our sample, where we differentiate between the two subsets by color. Green data points represent low-mass clusters, while orange data points represent larger clusters. We can see in this plot that large clusters' metallicity profiles are less scattered than low-mass clusters'. This translates in the different observed dispersions of $\bar{Z}_{in}$ seen in Figure 3.

Comparing CC and NCC clusters, we find that for CC clusters $\bar{Z}_{in} = 0.30 \pm 0.10 Z_\odot$, while for NCC clusters $\bar{Z}_{in} = 0.37 \pm 0.080 Z_\odot$. We find that $\bar{Z}_{in}$ is larger for NCC clusters compared to CC clusters in this sample, despite the difference being within the measured dispersions of both quantities. This contrasts to the metal excess measured in the centers of CC cluster in e.g. De Grandi & Molendi (2001).

3.2.3. *Outer Metallicity, $\bar{Z}_{mid}$*

The measured values of $\bar{Z}_{mid}$ are shown in Table F1, in Appendix F. In Figure 5, we show a plot of $\bar{Z}_{mid}$, which measures the average metallicity outside the core, as a function of the total mass, M_{500}, and as a function of kT_X. In Table 3, we show the statistics for the distribution of $\bar{Z}_{mid}$ values. In the case of outer metallicity, we no longer detect a clear difference in the dispersions of high- and low-mass clusters. However, when we compare $\bar{Z}_{mid}$ to $\bar{Z}_{in}$, we find that for each of the low- and high-mass cluster samples, $\bar{Z}_{mid}$ values are smaller than $\bar{Z}_{in}$ values. For high-mass clusters, for example, the mean and standard deviation for $\bar{Z}_{mid}$ are $(0.27 \pm 0.073) Z_\odot$, while for $\bar{Z}_{in}$ they are $(0.36 \pm 0.050) Z_\odot$. This points to a decrease in the iron mass fraction as we move from the core region, $r < 0.15 R_{500}$, to the outer region $0.15 < r < 0.3 R_{500}$. This decrease is however within the measured dispersions of $\bar{Z}_{mid}$ and $\bar{Z}_{in}$ and is also found for low-mass clusters.

TABLE 3: Statistics for $\bar{Z}_{mid}$.

	Model	Mean ($Z_\odot$)	Std. Dev. ($Z_\odot$)	χ^2/dof
$M_{500} < 3.5 \times 10^{14} M_\odot$	1T	0.22	0.079	10. (150./15)
	2T	0.20	0.085	9.1 (140./15)
$M_{500} > 3.5 \times 10^{14} M_\odot$	1T	0.27	0.073	3.2 (79./25)
	2T	0.27	0.074	2.3 (56./25)

Note. — Error-weighted mean, standard deviation of $\bar{Z}_{mid}$ and χ^2/dof with respect to calculated mean. Results shown for clusters with M_{500} smaller than and larger than $3.5 \times 10^{14} M_\odot$, and for fits using the 1T and the 2T spectral models

3.3. *Metallicity-Entropy Relation*

One direct approach to look for a relation between pre-enrichment and pre-heating is to look for a correlation between the ICM non-gravitational entropy and the ICM bulk metallicity measured outside the central region of the cluster, $\bar{Z}_{mid}$. In addition, we also consider the relation between non-gravitational entropy and $\bar{Z}_{in}$. We use the ratio of measured entropy to the expected gravitational entropy, S_{grav}, to probe the amount non-gravitational entropy. We define the scaled entropy $x_s \equiv S/S_{grav}$, which we use as a measure for any non-gravitational entropy, and discuss our assumptions on S_{grav}, below.

The metallicity-entropy relation is studied with entropy measured at several locations in the clusters. First, we consider entropy measurements at fixed R_{500}-scaled radii. This is justified because the gravita-

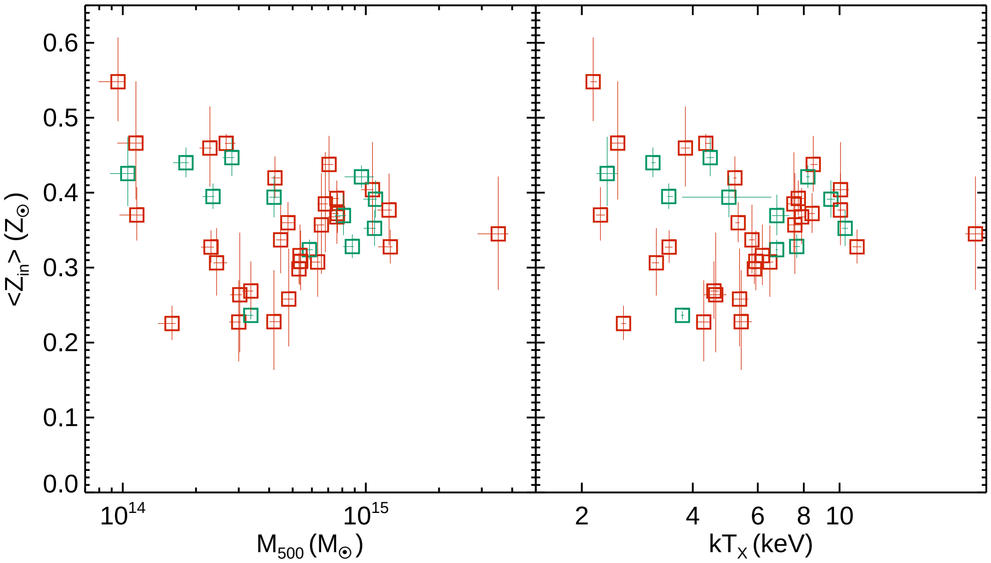

FIG. 3: Core metallicity as a function of cluster mass or temperature. *Left:* $\bar{Z}_{in}$ vs. M_{500}. *Right:* $\bar{Z}_{in}$ vs. kT_X. Red points are for NCC clusters, while turquoise points are for CC clusters.

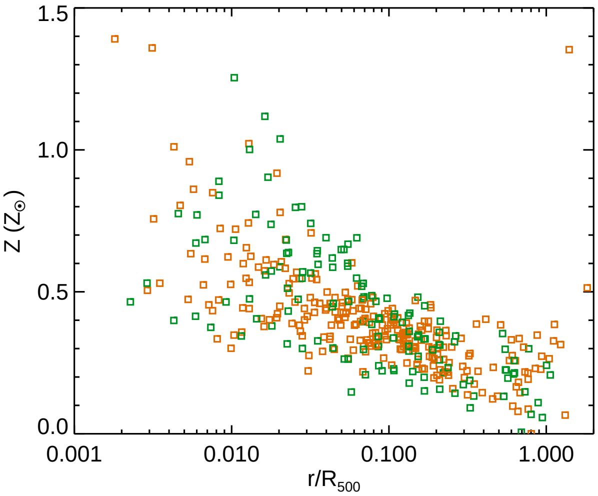

FIG. 4: Superimposed metallicity profiles of clusters. Orange data points are for clusters with mass $M_{500} > 3.5 \times 10^{14} M_\odot$, while green data points correspond to clusters with $M_{500} < 3.5 \times 10^{14} M_\odot$

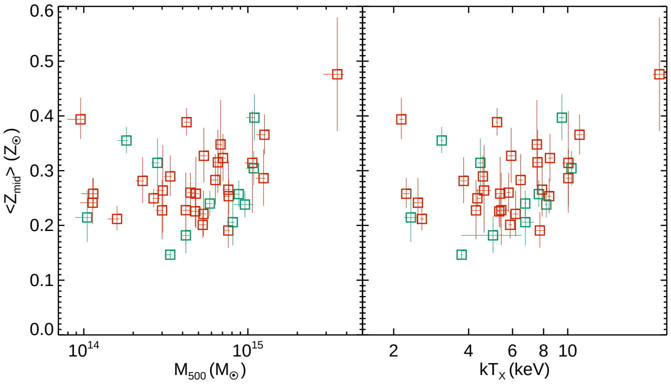

FIG. 5: Outer metallicity as a function of cluster mass or temperature. *Left:* $\bar{Z}_{mid}$ vs. M_{500}. *Right:* $\bar{Z}_{mid}$ vs. kT_X. Red points are for NCC clusters, while turquoise points are for CC clusters.

tional entropy model of Voit et al. (2005) scales self-similarly, and is given in terms of a profile which is a function of r/R_{500}. In this case, we define S_{grav} as the expected gravitational entropy from Voit's model, $S_{grav}(r) = S_V(r)$. Second, we take a Lagrangian approach and study entropy at a fixed interior gas mass fraction, $F_g \equiv M_g/(f_b M_{500})$, where M_g is the interior gas mass (see e.g. Tozzi & Norman 2001; Voit et al. 2003; Nath & Majumdar 2011). This can be useful because buoyancy tends to order the ICM such that low-entropy gas finds its way to the bottom of the cluster potential, while high-entropy gas rises to large radii. In this latter case, we simply use $S_{grav} = S_{500}$ to scale the entropy, to avoid using a specific model of entropy dependence on F_g, while still capturing the S_{500} scaling expected in self-similar galaxy clusters.

In the analysis below not all clusters are included for each measurement. The first filter we apply is to exclude 4 clusters, which are visually judged to greatly deviate from spherical symmetry. These are Abell 754, Abell 2256, Abell 3376 and Abell 3667. In addition, in the successive measurements at different radii, below, we only include a cluster at a certain radius if the size of the FOV is larger than the radius of interest.

We start by looking at the $\bar{Z}_{mid} - x_s$ relation at constant scaled radius. As described above, in this case, $x_s = x_s(r) = S(r)/S_{grav}(r) = S(r)/S_V(r)$. We measure entropy at $r = 0.2R_{500}$, $0.3R_{500}$, $0.5R_{500}$, $0.8R_{500}$ and $1R_{500}$. Our measurements are shown in Figure 6. Similarly, we consider the same relation at fixed F_g. We choose values of F_g corresponding to the sample average across all clusters, at r = 0.2, 0.3, 0.5, 0.8 and $1R_{500}$. Table 4 shows the correspondence between scaled radius and the sample average gas mass fraction.

Our metallicity-entropy measurements at constant F_g are shown in Figure 7.

TABLE 4: Cluster sample average of F_g at various radii.

r/R_{500}	0.2	0.3	0.5	0.8	1.0
F_g	0.050	0.10	0.24	0.47	0.63

As can be seen in Figures 6 and 7, there is no visible correlation between our estimate of non-gravitational entropy, and the bulk metal content of a cluster, as estimated by $\bar{Z}_{mid}$.

As for metallicity measured in the core, $\bar{Z}_{in}$, we expect low-radius metallicity measurements to probe processes that occur after the collapse of the cluster. We repeat the analysis performed above, with $\bar{Z}_{in}$ instead of $\bar{Z}_{mid}$. Figure 8 shows plots of the measured inner metallicity, $\bar{Z}_{in}$, against the ratio of measured entropy to S_V, at the above-mentioned scaled radii. Again, there is only weak indication of a correlation between inner metallicity and x_s, at smaller radii. We perform statistical analysis using a bootstrap resampling method to calculate the significance of the correlation between the various metallicity and entropy measures. The lowest obtained p-values are of 1.3% and 2.0% for the CC-only samples at $r = 0.3$ and $0.2R_{500}$, respectively.

4. DISCUSSION

4.1. *Inner Metallicity Scatter Systematics*

As was presented in Section 3.2.2, the core iron mass fraction, $\bar{Z}_{in}$, over our cluster sample has a different distribution for low-mass clusters than for high-mass clusters. Measurements of $\bar{Z}_{in}$ in large clusters ($M > 3.5 \times 10^{14} M_\odot$) are narrowly distributed around their mean of $0.36Z_\odot$, with a standard deviation of only $\sigma_Z = 0.050Z_\odot$. On the other hand, $\bar{Z}_{in}$ for low-mass clusters has a standard deviation of $\sigma_Z = 0.12Z_\odot$, around a slightly lower mean value for the sample. See Table 2 for details. The uncertainties on the individual $\bar{Z}_{in}$ measurements are too small to explain the dispersion in low-mass clusters, since $\chi^2/\text{d.o.f} = 33$. This means that the observed scatter is intrinsic to the data, and not a result of measurement uncertainties. On the other hand, we calculate $\chi^2/\text{d.o.f} = 2.6$ for $\bar{Z}_{in}$ in large clusters, indicating that measurement uncertainties contribute relatively more to the scatter, which nonetheless has a much lower value of only $\sigma_Z = 0.050Z_\odot$.

We attempt here to understand the difference between the distribution of low- and high-mass clusters' inner metallicity values. First we check whether the observed effect is due to systematics, and then we present several physical explanations of the measurements, in the following sections.

The first systematic effect to be tested concerns the inclusion of X-ray photons from the region $r > 0.15R_{500}$ in the computation of $\bar{Z}_{in}$. This occurs because spectral regions for metallicity measurement are defined before R_{500} is computed, while we desire for $\bar{Z}_{in}$ to measure the metallicity within $0.15R_{500}$. Once R_{500} is calculated, to compute $\bar{Z}_{in}$, we include all radial bins which overlap the disc $r < 0.15R_{500}$. The last such bin will, in general, extend beyond $r = 0.15R_{500}$. We address this by estimating the fraction of counts originating from the region $r > 0.15R_{500}$, which are used to compute $\bar{Z}_{in}$. We denote this count fraction by f_{out}, and show a histogram of its distribution in our sample in Figure 10.

Since metallicity profiles generally decrease with radius, including emission from large radii for a given cluster might bias its $\bar{Z}_{in}$ measurement, compared to the rest of the sample. We would like to test the magnitude of this effect. We thus repeat the measurement of $\bar{Z}_{in}$ dispersion with a sample which excludes clusters with significant contribution from $r > 0.15R_{500}$. We choose the cutoff value to be $f_{out} = 0.25$ to capture the peak of the distribution of clusters with $f_{out} < 0.25$ seen in Figure 10. We calculate the mean, dispersion and $\chi^2/\text{d.o.f}$ statistics as was done with the complete sample. The results are displayed in Table 5. We find that the difference between the high- and low-mass cluster samples still remains for dispersion and $\chi^2/\text{d.o.f}$. We thus conclude that the spectral bins' sizes do not have a large effect on this discrepancy in measured metallicity dispersions.

TABLE 5: Statistics for $\bar{Z}_{in}$ excluding clusters with $f_{out} > 0.25$.

	Model	Mean ($Z_\odot$)	Std. Dev. ($Z_\odot$)	χ^2/dof
$M_{500} < 3.5 \times 10^{14} M_\odot$	1T 2T	0.30 0.26	0.15 0.18	59. (470./8) 57. (460./8)
$M_{500} > 3.5 \times 10^{14} M_\odot$	1T 2T	0.36 0.35	0.038 0.043	3.7 (49./13) 1.5 (19./13)

Note. — Similar to Table 2, using a cluster sample that excludes $f_{out} > 0.25$ clusters.

The second systematic effect we test is the effect of the number of radial bins used to measure $\bar{Z}_{in}$ in the obtained value. As can be seen in Equation 8, $\bar{Z}_{in}$ is a weighted sum of single metallicity measurements. For clusters without enough photons to create multiple radial bins within $0.15R_{500}$, the measurements will give less precise estimates of $\bar{Z}_{in}$, on average. We find, however, that there is no significant dependence of $\bar{Z}_{in}$ on the number of bins used to estimate it. In addition, we also find that the number of bins covering $r < 0.15R_{500}$ does not depend on M_{500}.

We also repeat the analysis using a constant physical radius aperture of 150kpc to compute the inner iron mass fraction. We find that the different levels of dispersion remain unchanged, even with the physical radius aperture.

4.2. *Metallicity Scatter as a Reflection of Structure Formation*

One possible physical explanation to this observed difference between low-mass and high-mass clusters, is that the metal content in clusters is driven by the merger history of clusters. In the hierarchical model of structure formation, low-mass clusters, groups and galaxies merge to form the larger-mass clusters. Thus, if the metal content is non-uniform across all these progenitors, as they merge with each other, the resulting metallicity is an average of the initial progenitor metallicities. In a simple

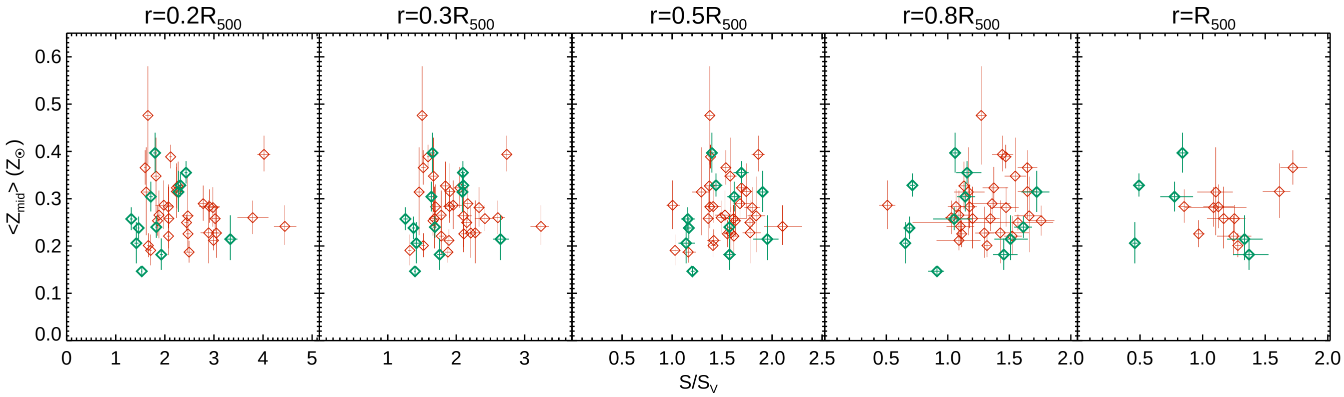

FIG. 6: Plot of gas mass-weighted metallicity $\bar{Z}_{mid}$, vs. the scaled entropy, S/S_V. Panels from left to right represent the cases where entropy is measured at $r = 0.2R_{500}$, $r = 0.3R_{500}$, $r = 0.5R_{500}$, $r = 0.8R_{500}$ and $r = R_{500}$. Only clusters with *Chandra* coverage at each of these radii are represented in the corresponding panel. Turquoise data points are for CC cluster, while red points represent NCC clusters. Abell 400 is the outlying cluster with large metallicity at $\bar{Z}_{mid} \sim 0.6Z_\odot$.

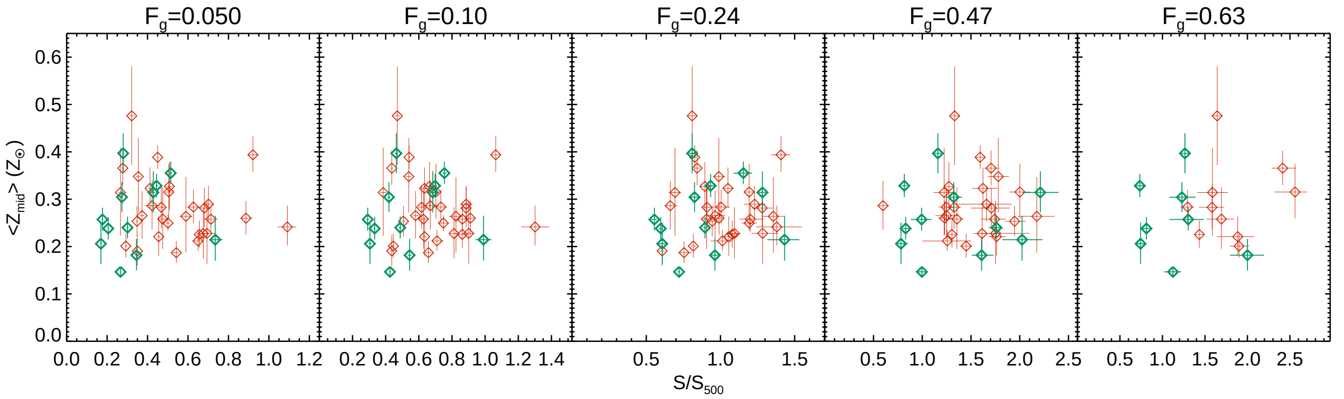

FIG. 7: Plot of gas mass-weighted metallicity $\bar{Z}_{mid}$, vs. the scaled entropy, S/S_V. Panels from left to right represent the cases where entropy is measured at $F_g = 0.050$, $F_g = 0.10$, $F_g = 0.24$, $F_g = 0.47$ and $F_g = 0.63$. Only clusters with *Chandra* coverage at each of these radii are represented in the corresponding panel. Turquoise data points are for CC cluster, while red points represent NCC clusters. Abell 400 is the outlying cluster with large metallicity at $\bar{Z}_{mid} \sim 0.6Z_\odot$.

model, if the metallicities of these progenitor structures are distributed around a mean universal value, Z_0, then the sum metal content in a cluster formed by the merger of all these components should approach Z_0, as the number of components increases. The iron mass fraction, $\bar{Z}_{in}$, of a large cluster will thus be an average of the metallicities of its smaller progenitors.

Under this hypothesis, the decrease of the dispersion of $\bar{Z}_{in}$ as we go from low-mass clusters to high-mass clusters simply results from the mixing of low-mass clusters' gas, after they merge to make larger clusters. The mixing then results in averaged, less dispersed metallicity values in the merged clusters, compared to the initial progenitors' metallicities. It must be noted, however, that a high mass cluster from our sample, say of $M_{500} \sim 10^{15} M_\odot$, will not be exclusively formed by the merger of $10^{14}M_\odot$-sized clusters, i.e from the low-mass extreme of our sample. A $10^{15}M_\odot$ cluster will undergo numerous mergers involving galaxy- and group-sized haloes, as well as a smooth and continuous accretion (see e.g. Fakhouri et al. 2010). This does not contradict the above hypothesis, as the more numerous the components making up a cluster are, the closer its metallicity approaches the universal average value.

If this is the correct explanation for the observed larger dispersion of $\bar{Z}_{in}$ in low-mass clusters, then it should also be reflected in the outer radii metallicity, $\bar{Z}_{mid}$, which is measured in the range $0.15 < r < 0.3R_{500}$. Our analysis however does not detect the same signal in the outer regions, as we do for inner metal content. The sample dispersion in $\bar{Z}_{mid}$ is roughly $0.079Z_\odot$ ($0.073Z_\odot$) for the low-mass (high-mass) sample, and the contribution of measurement uncertainties to that dispersion is estimated to be around $0.04Z_\odot$ ($0.05Z_\odot$) for the low-mass (high-mass) sample.

The decrease of the dispersion of *inner* metallicity from small to large clusters requires that, as clusters merge, metals from the progenitor clusters are able to efficiently find their way to the center of the cluster, while avoiding mixing with gas in the outer regions of clusters. Interestingly, the hydrodynamical simulations of Cora (2006) credit the infall of cold metal-rich clumps from large radii for the metal enrichment of the cluster central regions. A similar process is also one of the mechanisms evoked in Million et al. (2011) to explain the existence of a peak in the observed radial profiles of SNCC's metal prod-

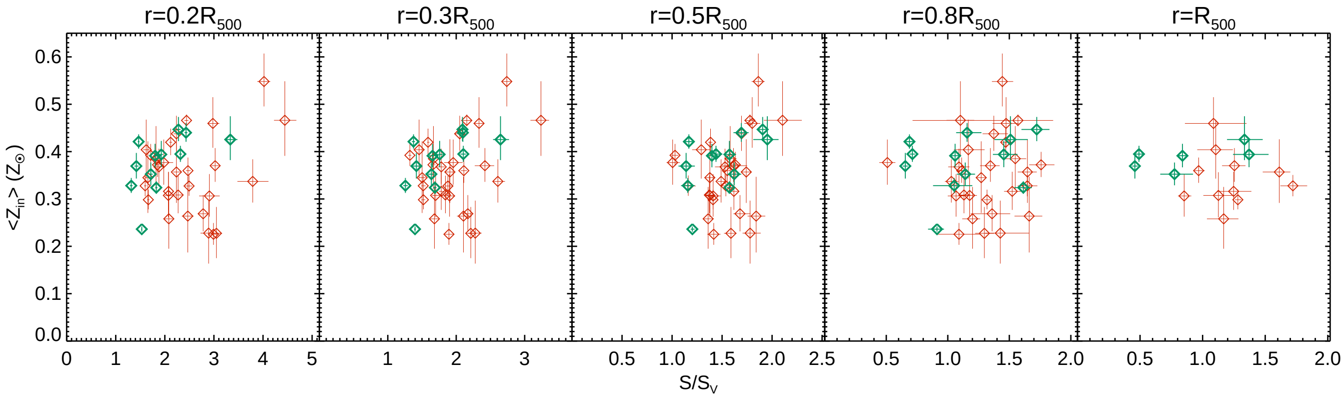

FIG. 8: Plot of gas mass-weighted metallicity $\bar{Z}_{in}$, vs. the scaled entropy, S/S_V. Panels from left to right represent the cases where entropy is measured at $r = 0.2R_{500}$, $r = 0.3R_{500}$, $r = 0.5R_{500}$, $r = 0.8R_{500}$ and $r = R_{500}$. Only clusters with *Chandra* coverage at each of these radii are represented in the corresponding panel. Turquoise data points are for CC cluster, while red points represent NCC clusters.

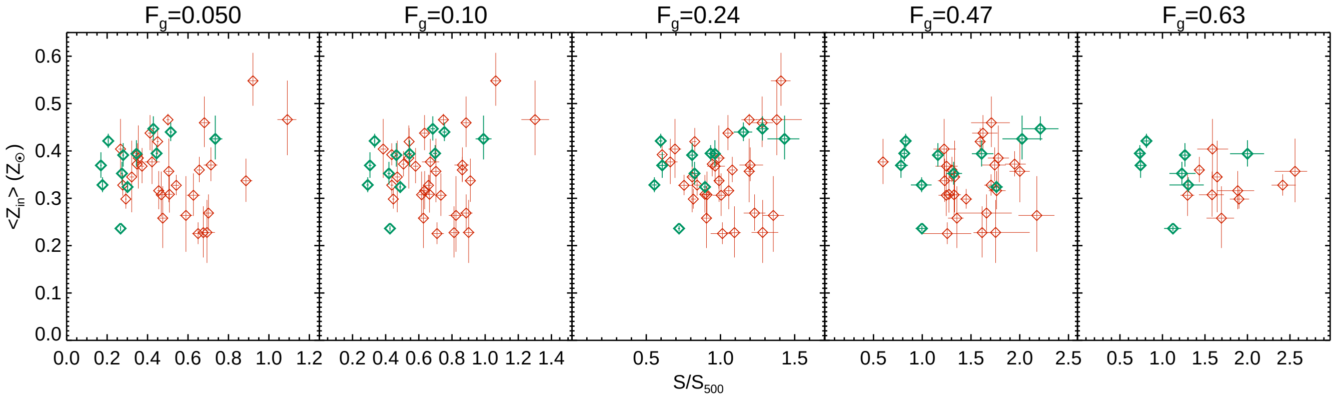

FIG. 9: Plot of gas mass-weighted metallicity $\bar{Z}_{in}$, vs. the scaled entropy, S/S_V. Panels from left to right represent the cases where entropy is measured at $F_g = 0.050$, $F_g = 0.10$, $F_g = 0.24$, $F_g = 0.47$ and $F_g = 0.63$. Only clusters with *Chandra* coverage at each of these radii are represented in the corresponding panel. Turquoise data points are for CC cluster, while red points represent NCC clusters.

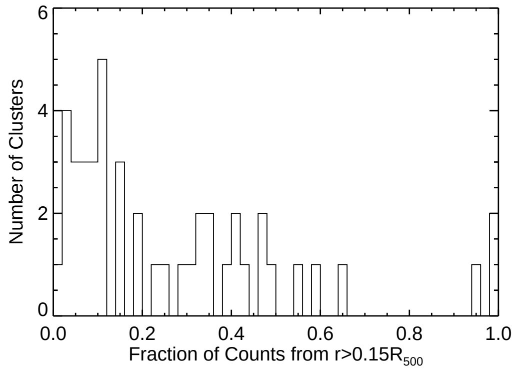

FIG. 10: Distribution of the values of f_{out} from the ensemble of $\bar{Z}_{in}$ measurements. See the text in Section 4.1 for a description of f_{out}.

ucts, also observed in e.g. Sanders & Fabian (2006), Simionescu et al. (2009a) and Simionescu et al. (2010). Metal-rich gas from a small cluster, or from a galaxy, merging into a larger one can avoid mixing with the bulk ICM at large radii if its entropy is low enough to allow it to pierce through the outer ICM and reach the center of the cluster. In addition, the absense of this discrepancy in the outer regions of clusters could imply that metals in the outer regions come from a source with a more uniform metallicity level, i.e. a source whose metallicity varies less from cluster to cluster. Such a homogeneous source could be the gas that is accreted very early in the formation of clusters, and whose metal contribution is generally referred to as pre-enrichment, which we further discuss in Section 4.3. Along the same lines, a slightly different interpretation of this finding is that, as time goes by, the haloes that merge later tend to have a wider distribution of metallicities, than those that merge earlier.

The hypothesis that merger statistics is behind the observed metallicity distribution across clusters can be tested in models that combine the statistics of structure formation with metal production in merging haloes, using a semi-analytical approach. Such a model was built in Elkholy (2012) to test other aspects of cluster chemical and dynamical histories, and can be adapted to test whether such observations can be reproduced semi-analytically.

We provide here, however, a very crude test of the above hypothesis. We would like to test whether the metallicities of clusters formed through the mergers of low-mass clusters from our sample have a similar distribution to that of metallicities of our high-mass clusters. To this end, we start by computing the metallicity $\bar{Z}_{in}$ resulting from the merger of two clusters from the sample of clusters in Figure 3 with $M_{500} < 3.5 \times 10^{14} M_{\odot}$. We draw any two clusters from the low-mass subset, and define the metallicity resulting from their merger as the gas-mass–weighted average of the $\bar{Z}_{in}$ values of the two merging clusters. The gas mass used in weighting the average is that measured within $0.15R_{500}$, from the data. The resulting metallicity is assigned to a mass, M_{500}, which is the sum of the masses of the merging clusters. This is repeated with three-, four-, five- and six-cluster mergers, again based on our $\bar{Z}_{in}$ measurements in low-mass clusters. Our generated metallicity distribution thus comes from all possible mergers between 6 or less clusters from our low-mass clusters sample.

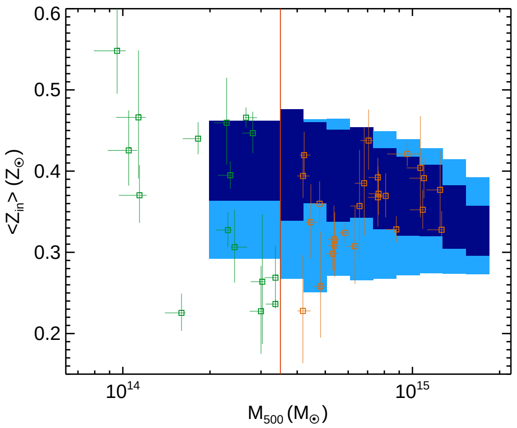

FIG. 11: The width of the metallicity distribution, resulting from the hypothetical merger of low-mass clusters from our sample. The light (dark) blue region represents the 95% (68%) spread of generated metallicities. The green and orange data points represent our measurements in low- and high-mass clusters, respectively. The vertical line is plotted at $M_{500} = 3.5 \times 10^{14} M_{\odot}$, and separates the above 2 samples.

Figure 11 shows the result of the above simulation, superimposed on our data points. We recover qualitatively the trend in our data, whereby the width of the distribution of clusters' metallicities decreases with mass. Beyond this toy model, a model incorporating more detailed statistics of structure formation, as well as a more sophisticated model for metal content in merging clusters, is required to lend support to the hypothesis linking our metallicity measurements to structure formation.

4.3. *Support for Pre-Enrichment?*

We argue above that the fact that metallicity dispersion as a function of cluster mass is not observed to change in the outer regions, while it does vary in inner regions can be explained if, outside the cluster core, most of the metals are the result of pre-enrichment, which is the metallicity level set before cluster formation (e.g. Fujita et al. 2008; Matsushita et al. 2013; Werner et al. 2013). The pre-enriched gas would have an approximately universal metallicity level, compared to the cold infalling haloes contributing metals at later times, whose gas metallicity values are more diverse.

We find another clue pointing to this initial pre-enrichment metallicity level — presumed to be the same for all clusters — when we compare $\bar{Z}_{in}$ values to the stellar-to-gas mass fractions in clusters. Dai et al. (2010) measure the stellar and baryon mass fractions of clusters with temperatures $1 \lesssim kT_X \lesssim 10$ keV, using 2MASS data for optical measurements, and *ROSAT* data for X-ray measurements. They measure a decreasing stellar-to-gas mass ratio, r_{sg}, as a function of cluster temperature, kT_X. Using the results of Dai et al. (2010), we can thus estimate the stellar mass from the X-ray temperature of a cluster and test whether it correlates with the metallicity of the ICM. A correlation is expected if the population of stars producing the metals detected in X-ray is the same as the one producing the optical luminosity of galaxies.

Dai et al. (2010) fit the temperature–stellar-mass trend to a power-law and obtain the following best-fit relation:

$$\log(r_{sg}) = -0.65 - 1.03 \log\left(\frac{kT_X}{1\mathrm{keV}}\right) . \qquad (14)$$

Now, we recall that $\bar{Z}_{in} = M_{Fe}^{in}/(A_{Fe} M_{gas}^{in})$, where M_{Fe}^{in} and M_{gas}^{in} are the iron and gas masses interior to $r = 0.15R_{500}$, respectively, and A_{Fe} is the solar iron abundance. We can then write

$$\bar{Z}_{in} = \frac{M_* \langle M_{Fe}/M_* \rangle}{M_{gas}^{in} A_{Fe}}, \qquad (15)$$

where M_* is the stellar mass of the cluster, and $\langle M_{Fe}/M_* \rangle$, the average iron mass in the ICM per stellar mass. Or, defining $Z_{eff} = \langle M_{Fe}/M_* \rangle / A_{Fe}$, this becomes

$$\bar{Z}_{in} = Z_{eff} r_{sg} \left(kT_X\right) \ , \qquad (16)$$

where Z_{eff} is the average iron mass in the ICM per stellar mass, scaled by the solar iron abundance, A_{Fe}. The assumption here is that Z_{eff} will be the same for all clusters, and will not depend on kT_X.

If we assume that all the iron inside $0.15R_{500}$ has been produced by the stars in the galaxies whose luminosities were used by Dai et al. (2010) to measure r_{sg}, above, or that at least a population of stars of mass proportional to M_* produced all the iron observed, then Equation 16 should describe the $\bar{Z}_{in} - kT_X$ data, once scaled by a suitable Z_{eff}.

We perform a least-squares fit of Equation 16 to the data. The purpose of this fit is not to estimate Z_{eff}, but simply to test whether the above picture is consistent with our data. We assume equal errors on metallicity measurements so that the results are not largely biased by the datapoints with smaller uncertainties. The best-fit model plotted in Figure 12, as the dashed yellow line, shows that Equation 16 is an inadequate fit to the observations. Similar to the conclusion in Bregman et al. (2010), this suggests that the stellar population producing the metals within $r = 0.15R_{500}$ is unlikely to be related to the currently observed galaxy population in clusters.

At the risk of having a model too flexible for our dataset, we thus introduce another parameter into Equa-

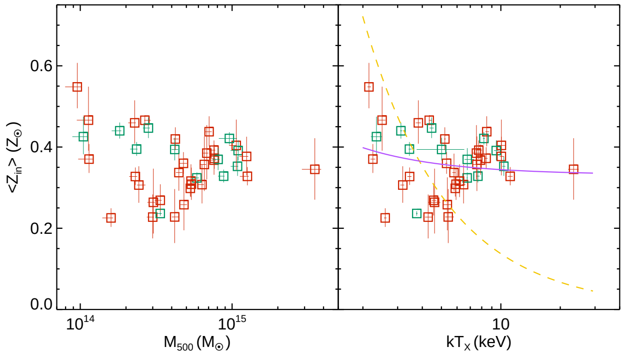

FIG. 12: *Left:* $\bar{Z}_{in}$ vs. M_{500}. *Right:* $\bar{Z}_{in}$ vs. kT_X. Red points are for NCC clusters, while turquoise points are for CC clusters. The yellow dashed line represent the $\bar{Z}_{in}-kT_X$ best-fit based on the stellar-to-gas mass ratio. The purple line is a similar fit based on stellar-to-gas mass ratio and assuming in addition a baseline pre-enrichment level.

tion 16, which is the mean metallicity in the ICM believed to have been set before the current galaxy population started adding more metals. We denote this initial metallicity by Z_{pre}. Our model then becomes

$$\bar{Z}_{in} = Z_{eff} r_{sg} \left(kT_X\right) + Z_{pre} \ . \tag{17}$$

Unlike Equation 16, Equation 17 fits the high-mass data better *and* passes near the middle of the wide distribution of metallicities of low-mass clusters. The best-fit is shown in Figure 12 as the purple line. This gives support to a mass-independent initial metallicity level in the cores of clusters. In this picture, larger clusters would have most of their core metals set by pre-enrichment, as $Z_{pre} \gg Z_{eff} r_{sg}$ for large kT_X. Conversely, smaller clusters would have a larger contribution from metals associated with stars, as $Z_{eff} r_{sg} \left(kT_X\right)$ increases at low kT_X. The best-fit model has a pre-enrichment value of $Z_{pre} \approx 0.3 Z_\odot$, and a $Z_{eff} \approx 2.Z_\odot$. While the value of Z_{pre} agrees with expectations, the large Z_{eff} value again points to the lack of observed galaxies, compared to the observed metals in clusters. The two fits above give similar results when repeated after excluding the bias-suspected clusters, i.e. clusters with $f_{out} < 0.25$.

4.4. *Inner Metallicity Boost During Mergers*

Finally, we test whether the dispersion in $\bar{Z}_{in}$ is related to dynamic activity, as measured by the centroid shift, $\langle w \rangle$, which is the size of the scatter of the X-ray centroid measured within various apertures around the X-ray peak (e.g. Mohr et al. 1993; O'Hara et al. 2006; Poole et al. 2006), and which is ideal for capturing merger activity (Poole et al. 2006). We find weak evidence for a $\bar{Z}_{in} - \langle w \rangle$ correlation, as we describe below.

Following the prescription in Poole et al. (2006), we calculate the position of the centroid of the X-ray emission within a radius of $0.3R_{500}$, and excluding the central 30kpc. We then calculate the centroid for apertures that are successively smaller by 5% of $0.3R_{500}$. For each aperture, i, we record the distance between calculated centroid and the X-ray peak, d_i. The centroid shift, $\langle w \rangle$, is then simply the standard deviation of the distances, d_i, scaled by R_{500}. We compute $\langle w \rangle$ for clusters with a FOV that covers $0.3R_{500}$ entirely. We find this radius to be a good compromise to include a large area and a good number of clusters. We show the computed $\langle w \rangle$ values in Table E1. Figure 13 shows a plot of $\bar{Z}_{in}$ vs. $\langle w \rangle$, in the right panel. We also include the same plot for $\bar{Z}_{mid}$, in the left panel of the figure. Datapoints corresponding to low-mass clusters are in green color to distinguish them from the high-mass cluster datapoints in orange.

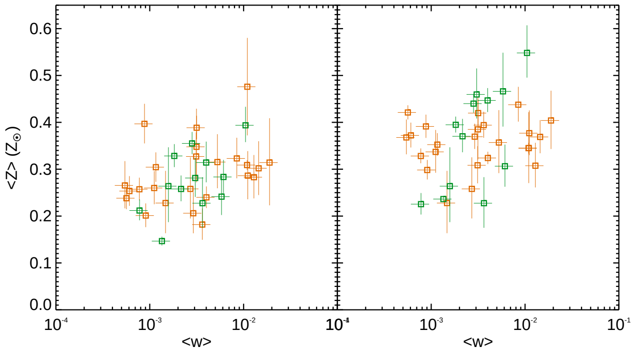

FIG. 13: *Left:* $\bar{Z}_{mid}$ vs. $\langle w \rangle$. *Right:* $\bar{Z}_{in}$ vs. $\langle w \rangle$. Green data points in either panel are for low-mass clusters, where $M_{500} < 3.5 \times 10^{14} M_\odot$. Orange data points are for $M_{500} > 3.5 \times 10^{14} M_\odot$ clusters.

Figure 13 suggests that there might be a correlation between $\bar{Z}_{in}$ and $\langle w \rangle$, for low-mass clusters. Pearson's product-moment correlation coefficient is found to be $r_P = 0.66$, with a p-value of 1.0% for the $\bar{Z}_{in} - \langle w \rangle$ correlation in clusters with $M_{500} < 3.5 \times 10^{14} M_\odot$.

This result suggests an alternative explanation to the $\bar{Z}_{in}$ dispersion in low-mass clusters, whereby mergers boost measured metallicity. This can be achieved in one of two ways. First, if mergers induce central AGN activity, then we might be observing metals distributed into the central cluster region by the central active engine, as was observed and described in e.g. Simionescu et al. (2009a,b); Kirkpatrick et al. (2009, 2011); O'Sullivan et al. (2011). This can also be the reason that we observe correlations between $\bar{Z}_{in}$ and the scaled entropy, x_s, as was shown in Section 3.3. Second, this enhanced central metallicity might simply be the measurement of the central metallicity peak of an infalling sub-cluster that is not completely merged with the main cluster, and whose emission is superimposed on the $r < 0.15R_{500}$ region of the main cluster. In both cases, these effects would need to have a stronger influence on metallicity in low-mass clusters compared to larger clusters.

4.5. *Searching for a Pre-Enrichment–Pre-Heating Link*

The motivation behind undertaking the study of metallicity and entropy as far as possible from the central region — where the influence of the central engine and the effects of cooling increase — was to search for the signature of supernovae (SNe), which have been heating and chemically enriching the gas surrounding them even before the formation of the galaxy clusters.

The plots of $\bar{Z}_{mid}$ vs. x_s in Section 3.3 show no hint of a relation between the two quantities. However, we note that for a given radius, the range of values for $x_s = S/S_{grav}$ can span a range as large as a factor of 3, at large radii. One can thus envision further study at such large radii to be applied to a larger sample of clusters, which is available in current *Chandra* archival data. A stacking technique can be used to look for trends between metallicity and excess entropy, and to lower any systematics due to the high X-ray background count fraction at such high radii. For example, we could group clusters in bins of S/S_{grav}, where S is measured at a large scaled radius, then extract spectra from each group of clusters from uniform R_{500}-scaled radial bins. These spectra could then be simultaneously fit, assuming they all have the same metallicity at a given scaled radial bin, and allowing for the temperatures to vary to match each cluster's temperature. Such study could be more sensitive to a potential weak trend between metallicity and excess entropy, pointing to the effects of early supernova enrichment and heat injection.

5. CONCLUSION

In this work, we analyze a sample of 46 galaxy clusters, extracting chemical and dynamical measurements, in the hopes of obtaining clues about the history of clusters. We measure entropy profiles out to the largest radii where temperature can be measured, and provide the best-fit temperature and density profiles for the community to use. We also measure metallicity profiles, for our cluster sample, and present them below. The data is made available on an FTP site[10].

We observe a difference in the scaled iron mass between the centers of low-mass clusters, and the centers of high-mass clusters: the values of the iron content in small clusters are more dispersed than those in large clusters. We suggest two possible interpretations of this observation:

1. The lower dispersion in the larger clusters may be a result of the averaging of metallicities from the larger number of haloes that have merged to form them. The fact that this effect can be seen even in the core of clusters lends support to the idea that the centers of clusters continue being enriched by cold and metal-rich gas, originating from the cluster outskirts, even at low redshift.
2. Alternatively, there are hints that clusters can undergo a boost of metallicity during a merger event, which can contribute to the enhancement of metallicity measured in low-mass clusters.

We also look for a connection between the bulk metal content of clusters and their dynamical state, as measured by the deviation of their entropy profiles from a self-similar profile, expected from gravitational shock heating, during cluster formation. We find no evidence of such relation in our data. More sophisticated studies using a larger sample would be required for such measurement to obtain more conclusive results.

TYE would like to thank Michael McDonald for very fruitful conversations.

---

[10] `ftp://space.mit.edu/pub/tamer/ebc2015/`

Bibliography

Anders, E. & Grevesse, N. 1989, Geochim. Cosmochim. Acta, 53, 197

Balestra, I., Tozzi, P., Ettori, S., Rosati, P., Borgani, S., Mainieri, V., Norman, C. & Viola, M. 2007, A&A, 462, 429

Borgani, S., Finoguenov, A., Kay, S. T., Ponman, T. J., Springel, V., Tozzi, P. & Voit, G. M. 2005, MNRAS, 361, 233

Borgani, S., Fabjan, D., Tornatore, L., Schindler, S., Dolag, K. & Diaferio, A. 2008, SSRv, 134, 379

Bregman, J. N. & Anderson, M. E. & Dai, X. 2010, ApJ, 716, 63

Cavagnolo, K. W., Donahue, M., Voit, G. M. & Sun, M. 2009, ApJS, 182, 12

Cora, S. A. 2006, MNRAS, 368, 1540

Dai, X., Bregman, J. N., Kochanek, C. S. & Rasia, E. 2010, ApJ, 719, 119

De Grandi, S. & Molendi, S. 2001, ApJ, 551, 153

Dickey, J. M. & Lockman, F. J. 1990, ARA&A, 28, 215

Elkholy, T. Y. 2012, PhD Thesis, Massachusetts Institute of Technology, `http://dspace.mit.edu/handle/1721.1/79425`

Fabjan, D., Tornatore, L., Borgani, S., Saro, A. & Dolag, K. 2008, MNRAS, 386, 1265

Fakhouri, O., Ma, C.-P. & Boylan-Kolchin, M. 2010, MNRAS, 406, 2267

Fujita, Y., Tawa, N., Hayashida, K., Takizawa, M., Matsumoto, H., Okabe, N. & Reiprich, T. H. 2008, PASJ, 60, 343

Kalberla, P. M. W., Burton, W. B., Hartmann, D., Arnal, E. M., Bajaja, E., Morras, R. & Pöppel, W. G. L. 2005, A&A, 440, 775

Kirkpatrick, C. C., Gitti, M., Cavagnolo, K. W., McNamara, B. R., David, L. P., Nulsen, P. E. J. & Wise, M. W. 2009, ApJ, 707, L69

Kirkpatrick, C. C., McNamara, B. R. & Cavagnolo, K. W. 2011, ApJ, 731, L23

Kravtsov, A. V., Vikhlinin, A. & Nagai, D. 2006, ApJ, 650, 128

Lloyd-Davies, E. J., Ponman, T. J & Cannon, D. B., 2000, MNRAS, 315, 689

Loewenstein, M. 2006, ApJ, 648, 230

Matsushita, K., Sakuma, E., Sasaki, T., Sato, K. & Simionescu, A. 2013, ApJ, 764, 147

Mazzotta, P., Rasia, E., Moscardini, L. & Tormen, G. 2004, MNRAS, 354, 10

Maughan, B. J., Jones, C., Forman, W. & Van Speybroeck, L. 2008, ApJS, 174, 117

McNamara, B. R. & Nulsen, P. E. J. 2007, ARA&A, 45, 117

Million, E. T., Werner, N., Simionescu, A. & Allen, S. W. 2011, MNRAS, 418, 2744

Mohr, J. J., Fabriant, D. G. & Geller, M. J. 1993, ApJ, 413, 492

Nagai, D., Kravtsov, A. V. & Vikhlinin, A. 2007, ApJ, 668, 1

Nagashima, M., Lacey, C. G., Baugh, C. M., Frenk, C. S. & Cole, S. 2005, MNRAS, 358, 1247

Nath, B. B. & Majumdar, S. 2011, MNRAS, 416, 279

O'Hara, T. B., Mohr, J. J., Bialek J. J. & Evrard, A. E. 2006, ApJ, 639, 64

O'Sullivan, E., Giacintucci, S., David, L. P., Vrtilek, J. M. & Raychaudhury, S. 2011, MNRAS, 411, 1833

Pointecouteau, E., Arnaud, M. & Pratt, G. W. 2005, A&A, 435, 1

Ponman, T. J., Cannon, D. B. & Navarro, J. F. 1999, Nature, 397, 135

Ponman, T. J., Sanderson, A. J. R. & Finoguenov, A. 2003, MNRAS, 343, 331

Poole, G. B., Fardal, M. A., Babul, A., McCarthy, I. G., Quinn, T. & Wadsley, J. 2006, MNRAS, 373, 881

Portinari, L., Moretti, A., Chiosi, C. & Sommer-Larsen, J. 2004 ApJ, 604, 579

Pratt, G. W. et al. 2010, A&A, 511, 85

Reiprich, T. H. & Böhringer H. 2002, ApJ, 567, 716

Renzini, A., Ciotti, L., D'Ercole, A. & Pellegrini, S. 1993, ApJ, 419, 52

Santos, J. S., Rosati, P., Tozzi, P., Böhringer H., Ettori, S. & Bignamini A. 2008, A&A, 511, 85

Sanders, J. S. & Fabian, A. C. 2006, MNRAS, 371, 1483

Short, C. J., Thomas, P. A. & Young, O. E. 2013, MNRAS, 428, 1225

Simionescu, A., Werner, N., Böhringer, H., Kaastra, J. S., Finoguenov, A., Brüggen, M. & Nulsen, P. E. J. 2008, A&A, 493, 409

Simionescu, A., Werner, N., Finoguenov, A., Böhringer, H. & Brüggen, M. 2009, A&A, 482, 97

Simionescu, A., Werner, N., Forman, W. R., Miller E. D., Takei, Y., Böhringer, H., Churazov, E. & Nulsen, P. E. J. 2010, MNRAS, 405, 91

Smith, R. K., Brickhouse, N. S., Liedahl, D. A. & Raymond, J. C. 2001, ApJ, 556, L91
Tornatore, L., Borgani, S., Dolag, K. & Matteucci, F. 2007, MNRAS, 382, 1050

Tozzi, P. & Norman, C. 2001, ApJ, 546, 63

Vikhlinin, A., Markevitch, M., Murray, S. S., Jones, C., Forman, W. & Van Speybroeck, L. 2005, ApJ, 628, 655

Vikhlinin, A. 2006, ApJ, 640, 710

Vikhlinin, A., Kravtsov, A., Forman, W., Jones, C., Markevitch, M., Murray, S. S. & Van Speybroeck, L. 2006, ApJ, 640, 691

Voit, G. M., Balogh, M. L., Bower, R. G., Lacey, C. G. & Bryan, G. L. 2003, ApJ, 593, 272

Voit, G. M., Kay, S. T. & Bryan, G. L. 2005, MNRAS, 364, 909

Werner, N., Durret, F., Ohashi, T. & Schindler, S. 2008, SSRv, 134, 337

Werner, N., Urban, O., Simionescu, A. & Allen, S. W. 2013, Nature, 502, 656

APPENDIX

A. ENTROPY PROFILES

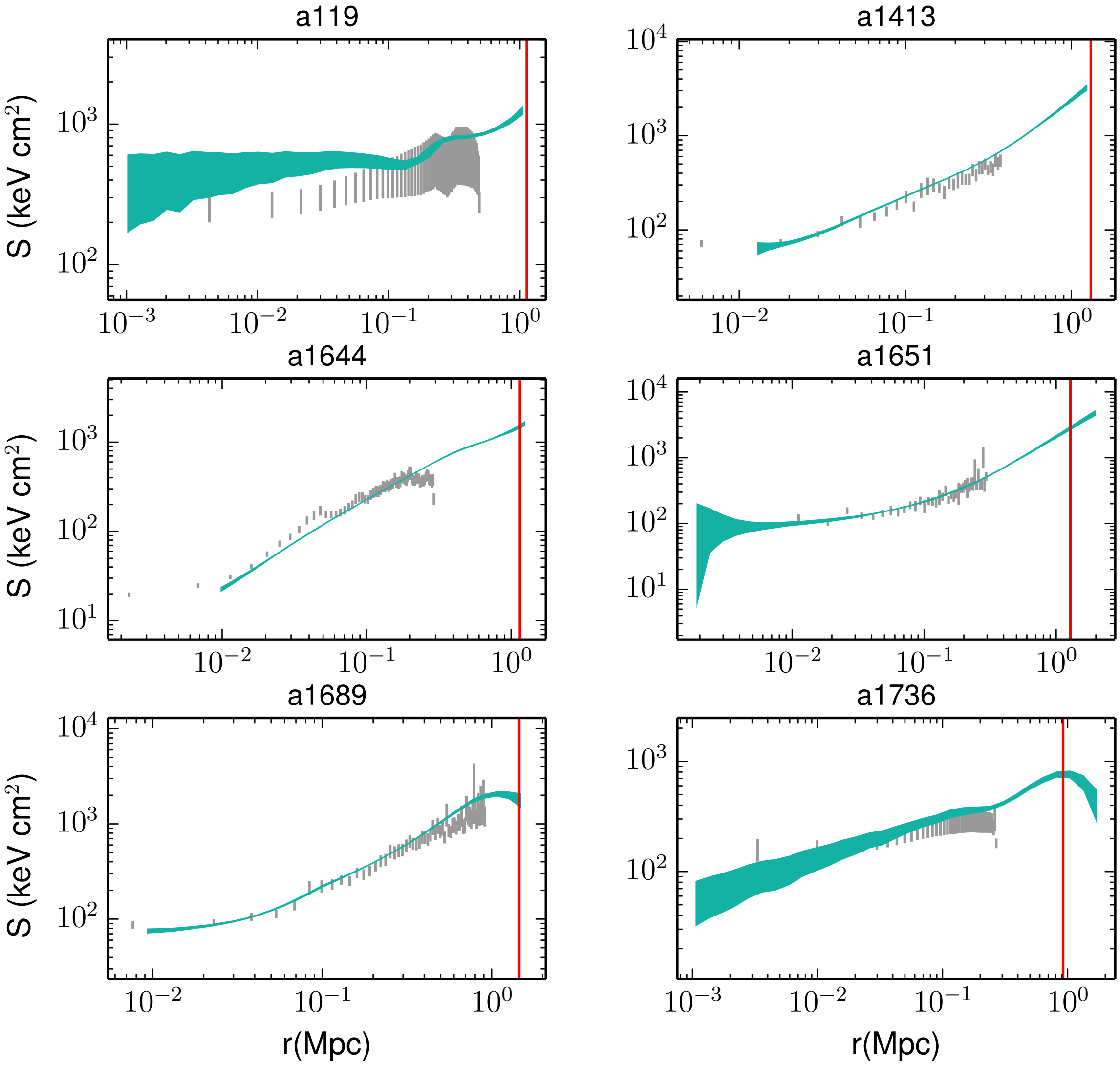

FIG. A1: Entropy profiles of the individual clusters in the sample. The turquoise area represents the 68% confidence region computed at various radii, from the temperature and density profiles produced by the Monte Carlo simulations described in Section 2.3.3. The gray error bars are the entropy profile measurements of the ACCEPT study, (Cavagnolo et al. 2009). See text for details. The vertical red line is drawn at $r = R_{500}$.

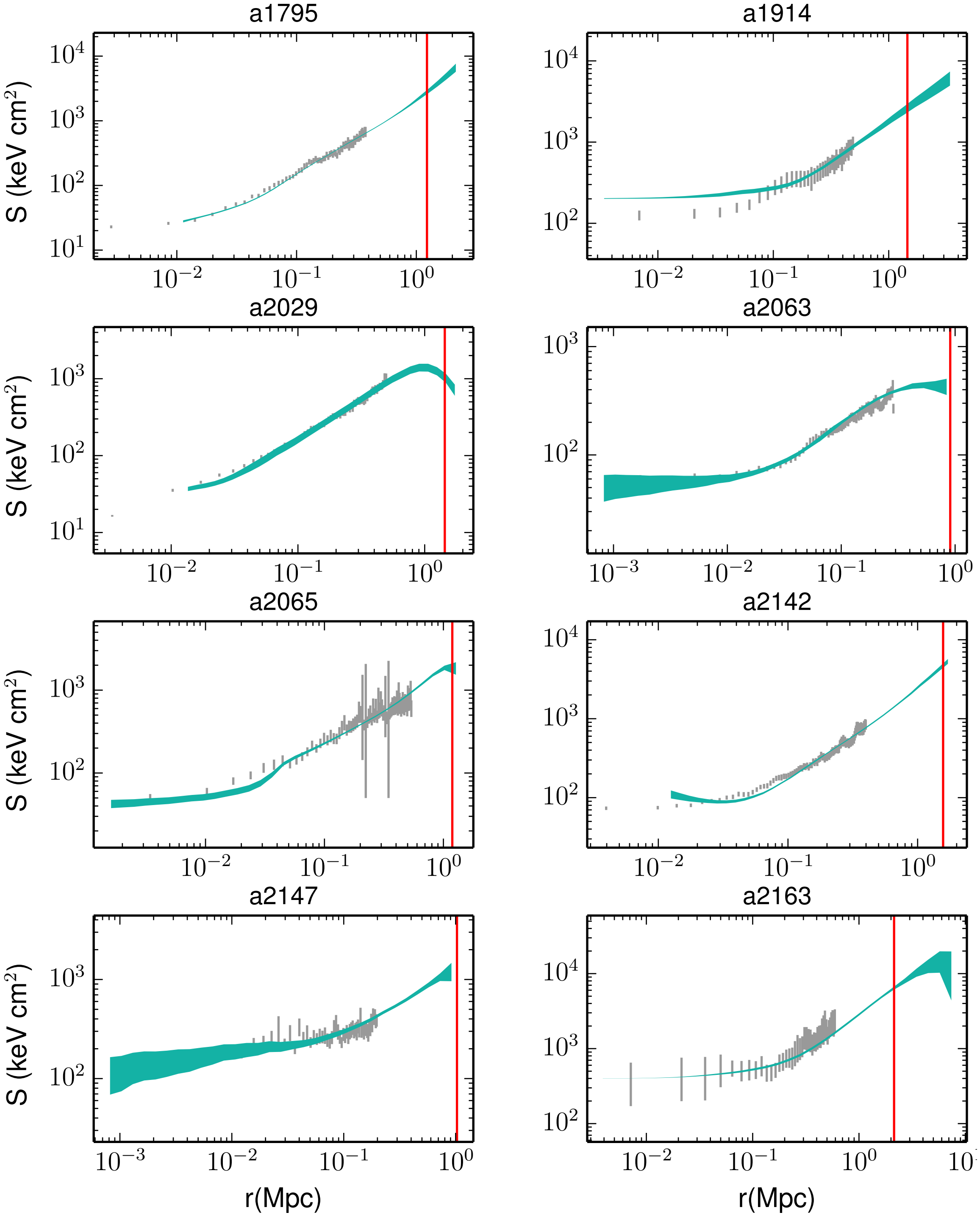

FIG. A1: *Continued.*

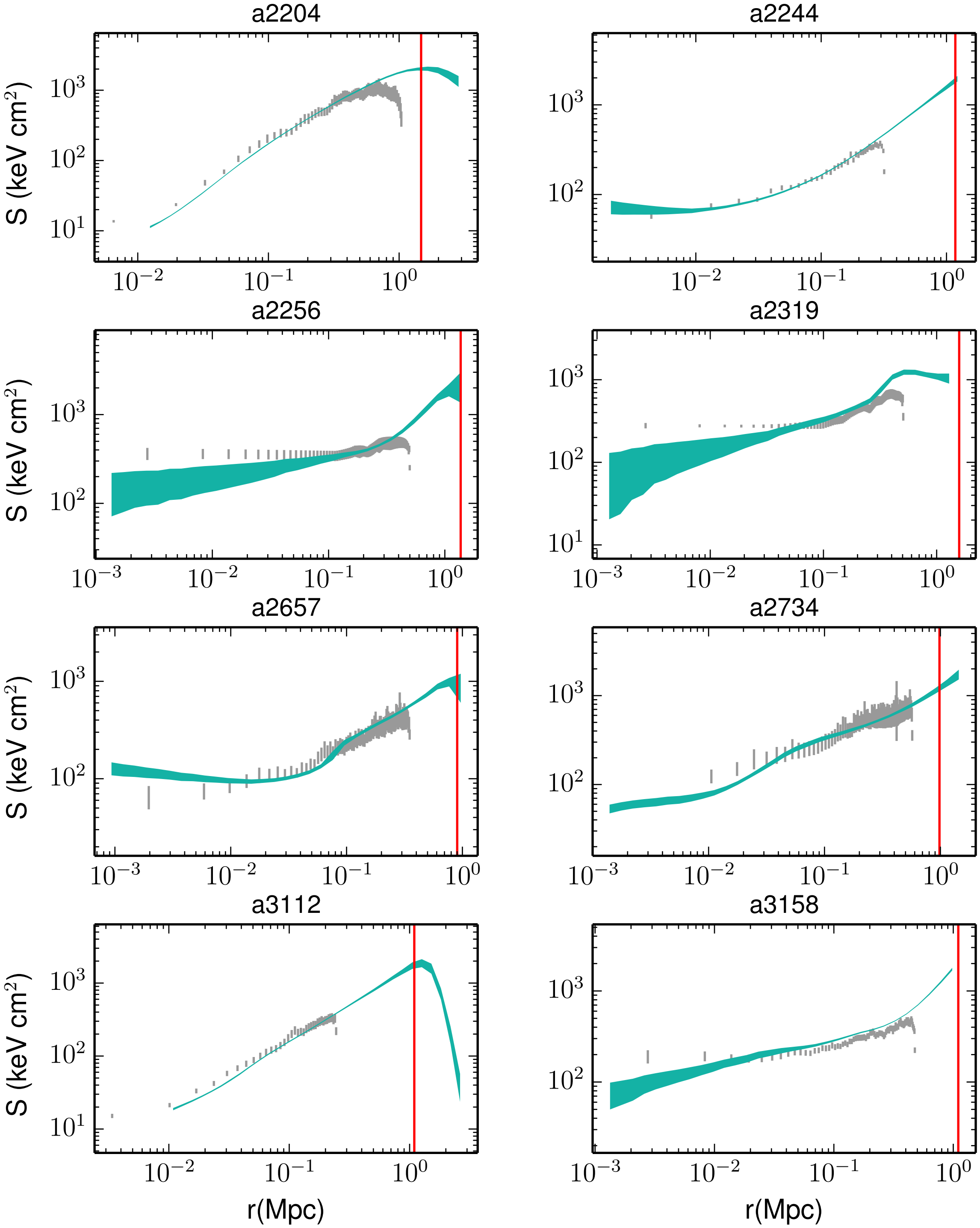

FIG. A1: *Continued.*

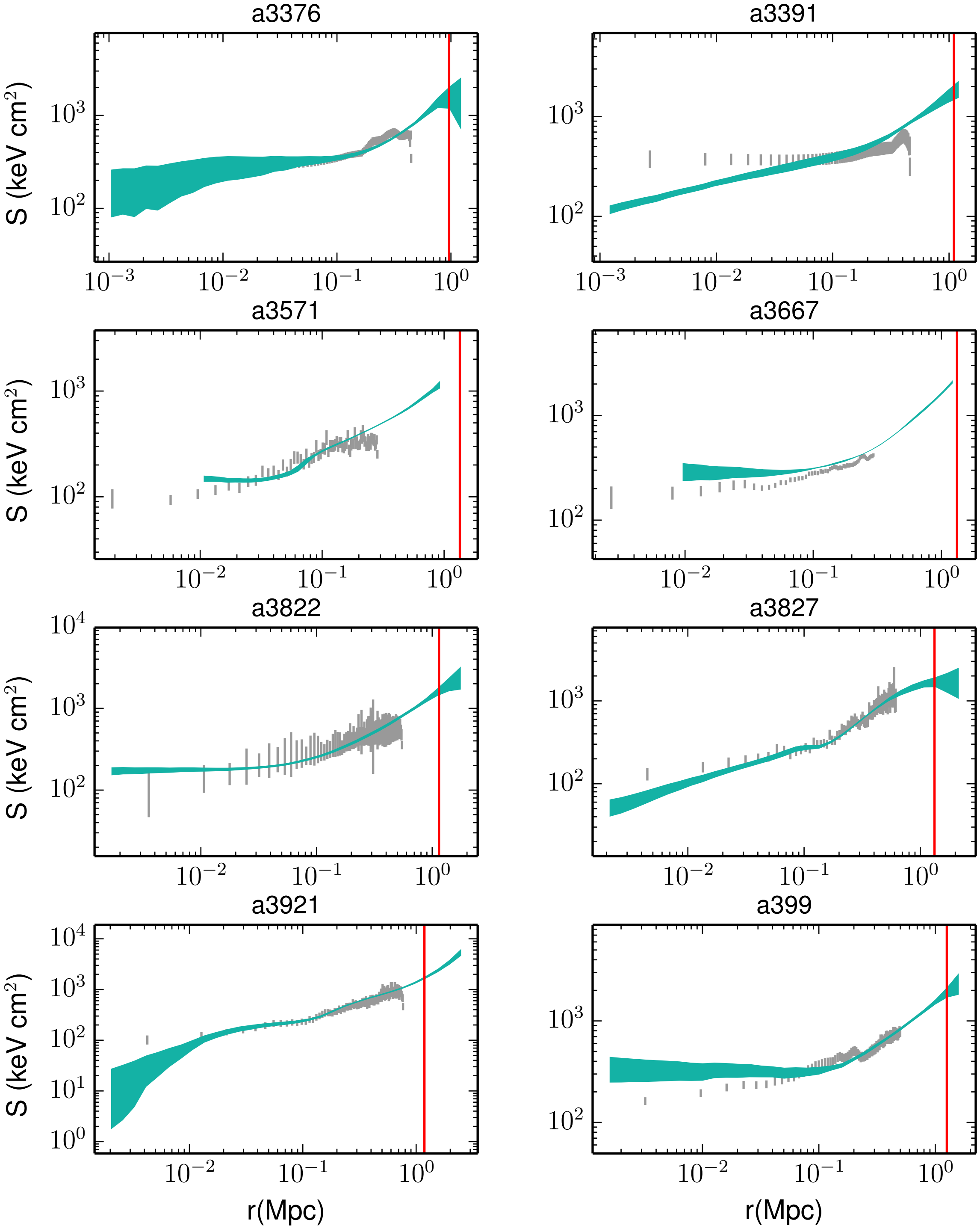

FIG. A1: *Continued.*

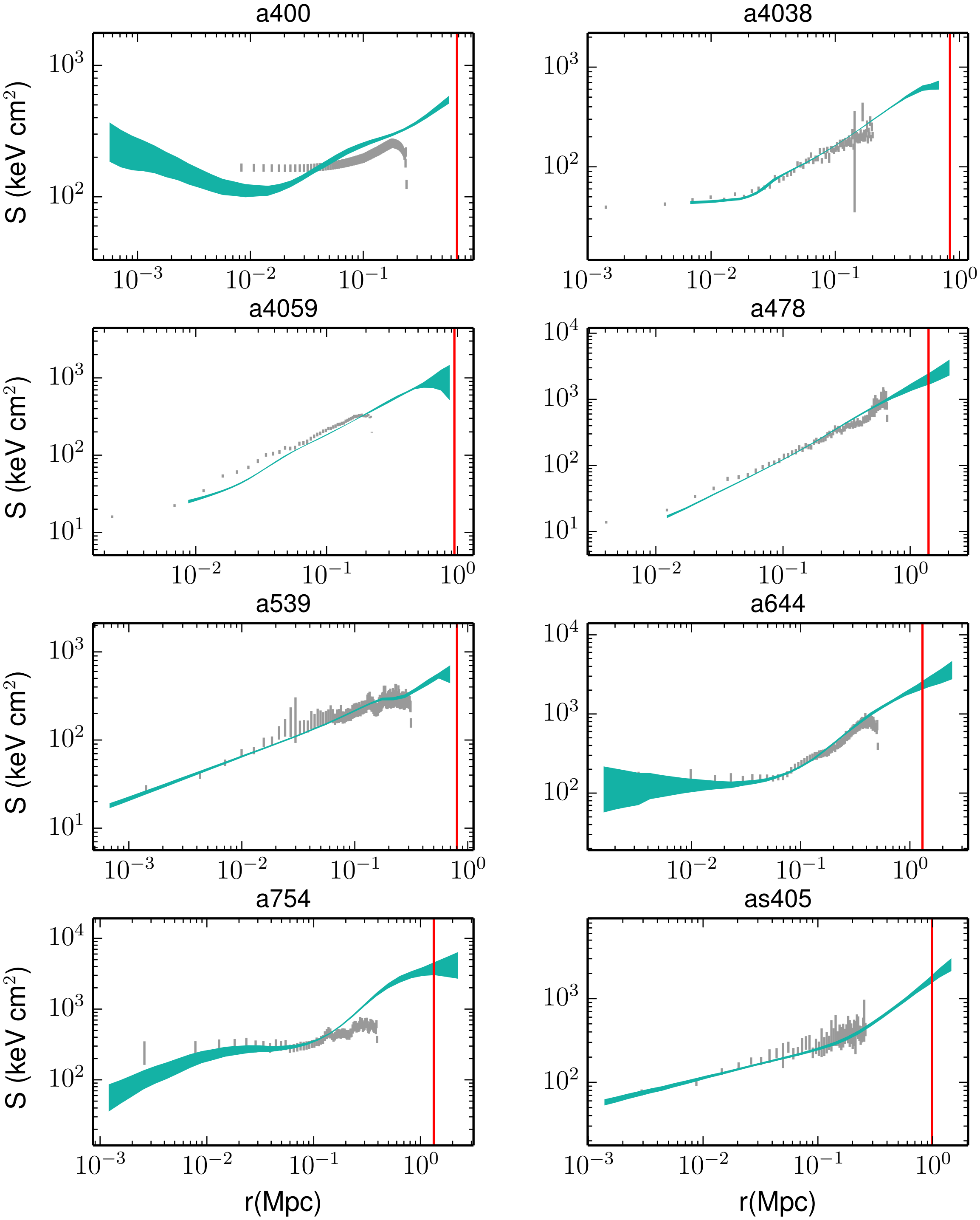

FIG. A1: *Continued.*

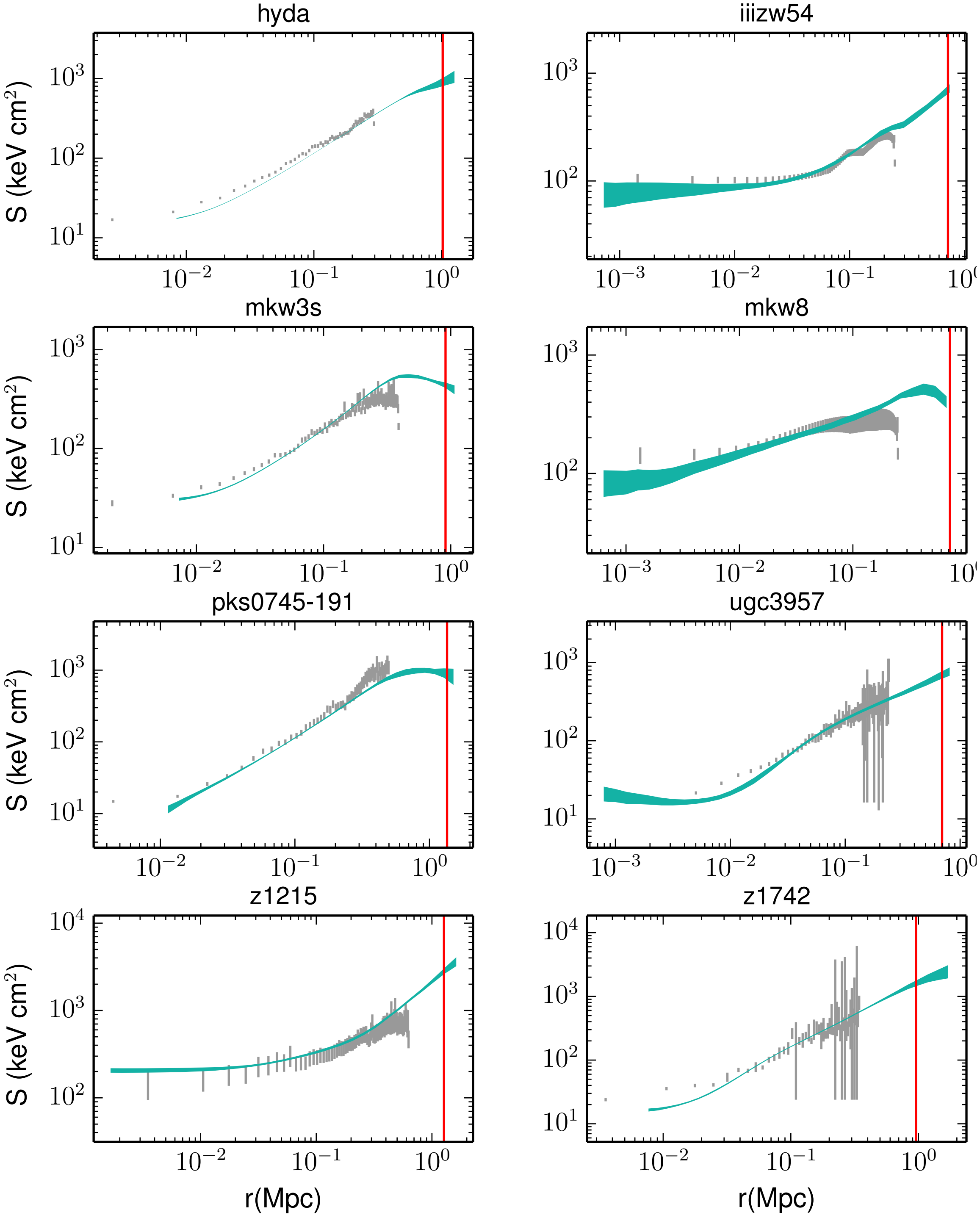

FIG. A1: *Continued.*

B. METALLICITY PROFILES

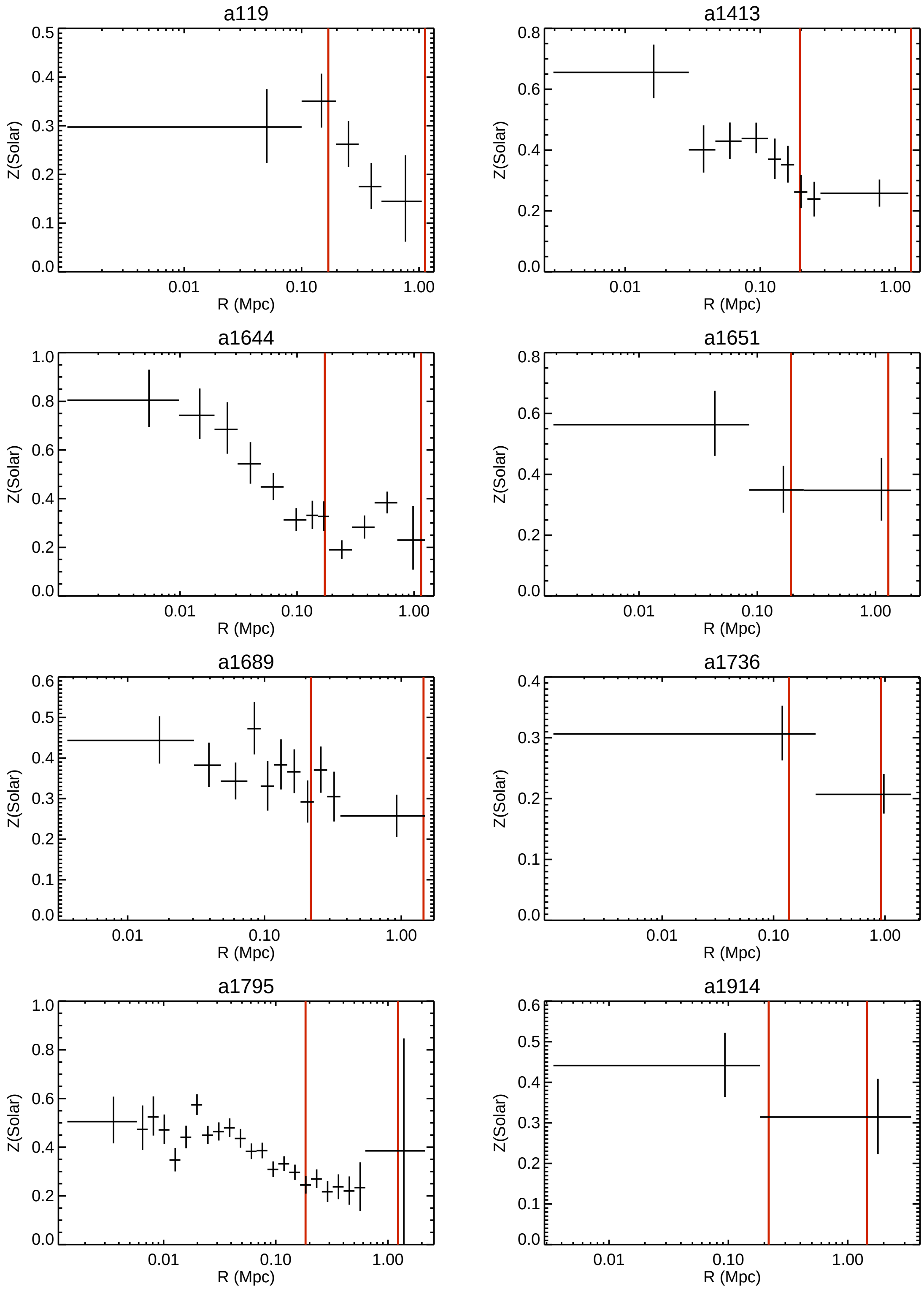

FIG. B1: Metallicity profiles of observed *Chandra* clusters. The two vertical red lines are drawn at $r = 0.15R_{500}$ and $r = R_{500}$. See Section 2.3.4 for the details of the metallicity measurement method.

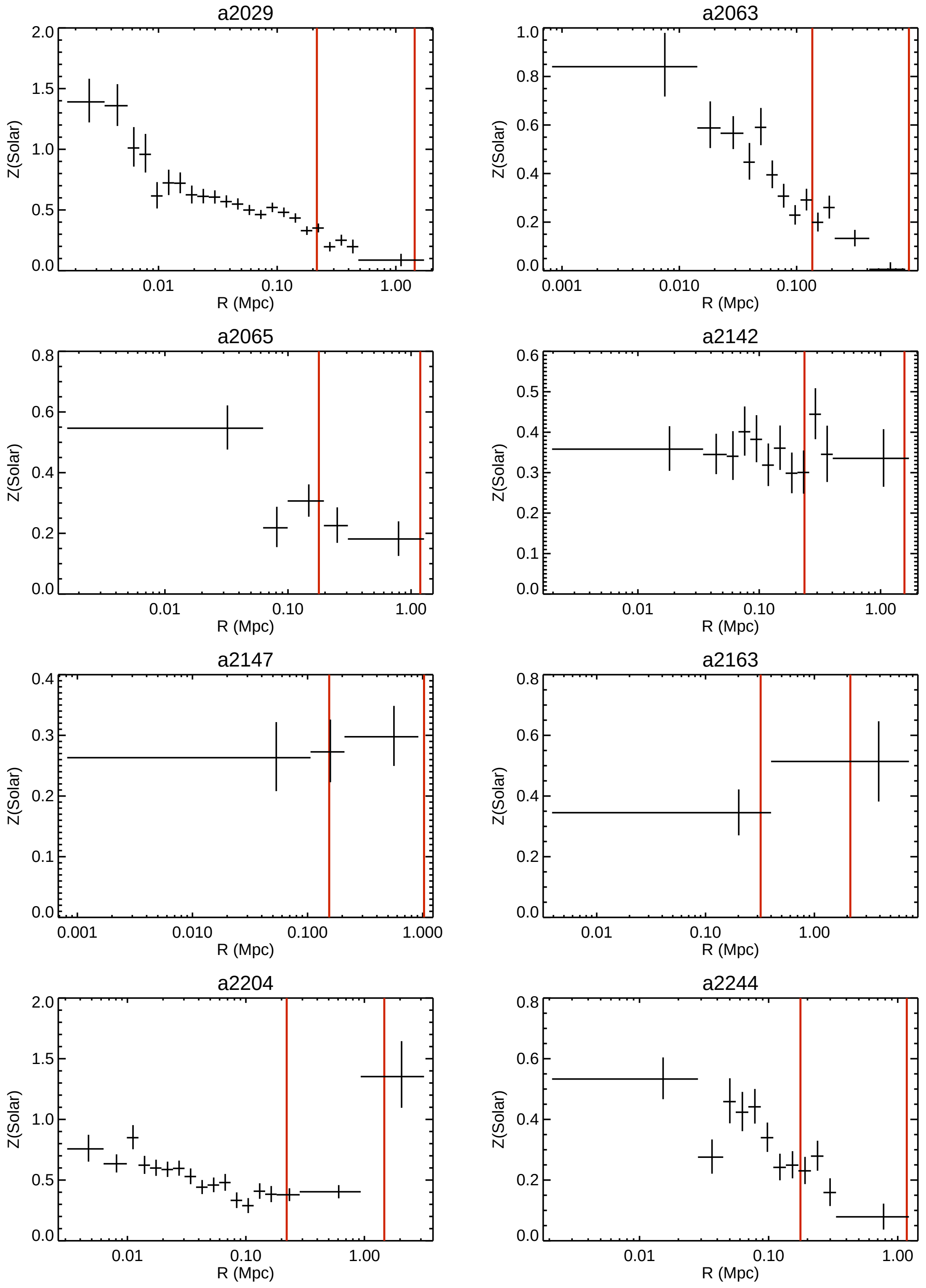

FIG. B1: *Continued.*

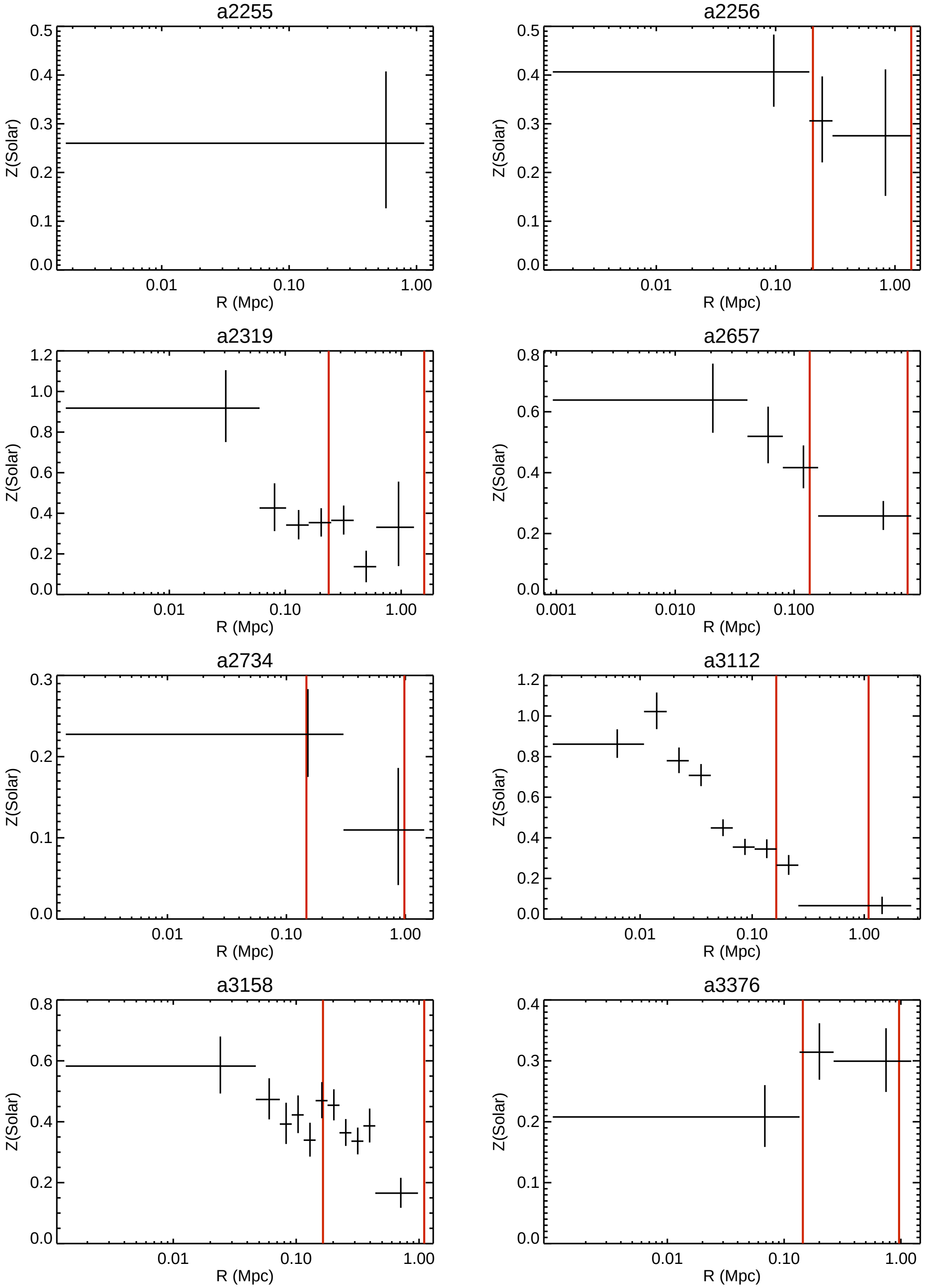

FIG. B1: *Continued.*

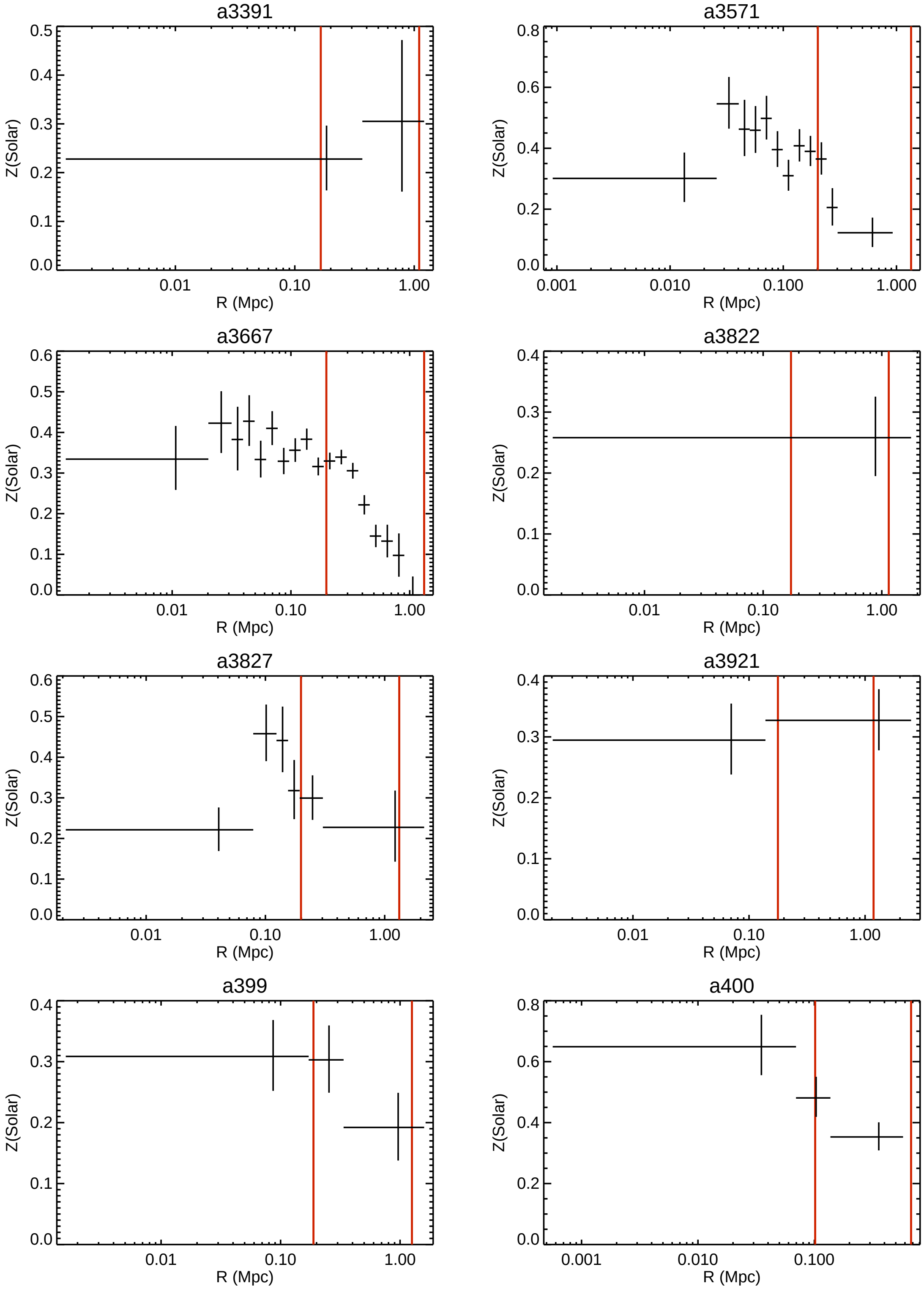

FIG. B1: *Continued.*

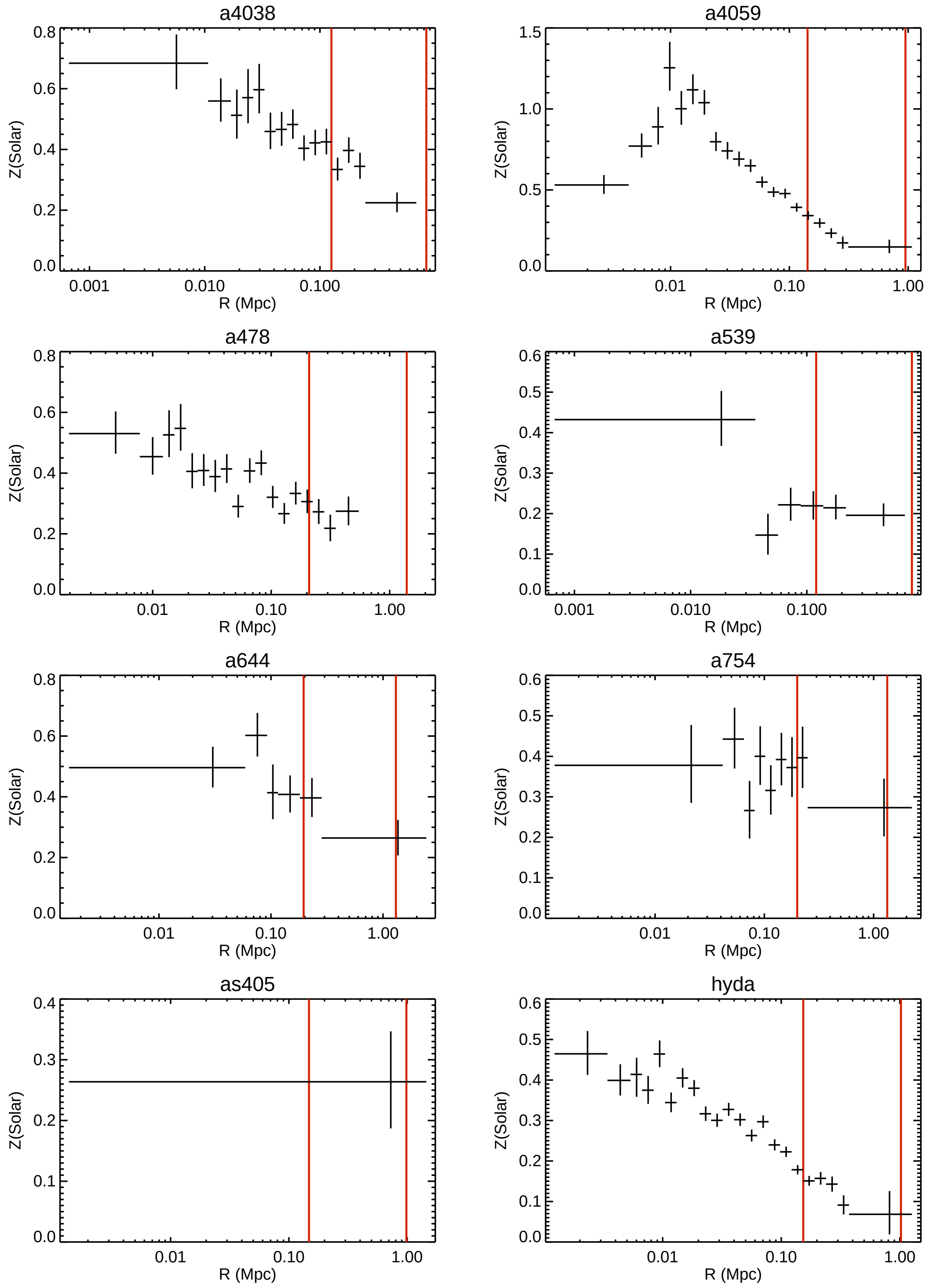

FIG. B1: *Continued.*

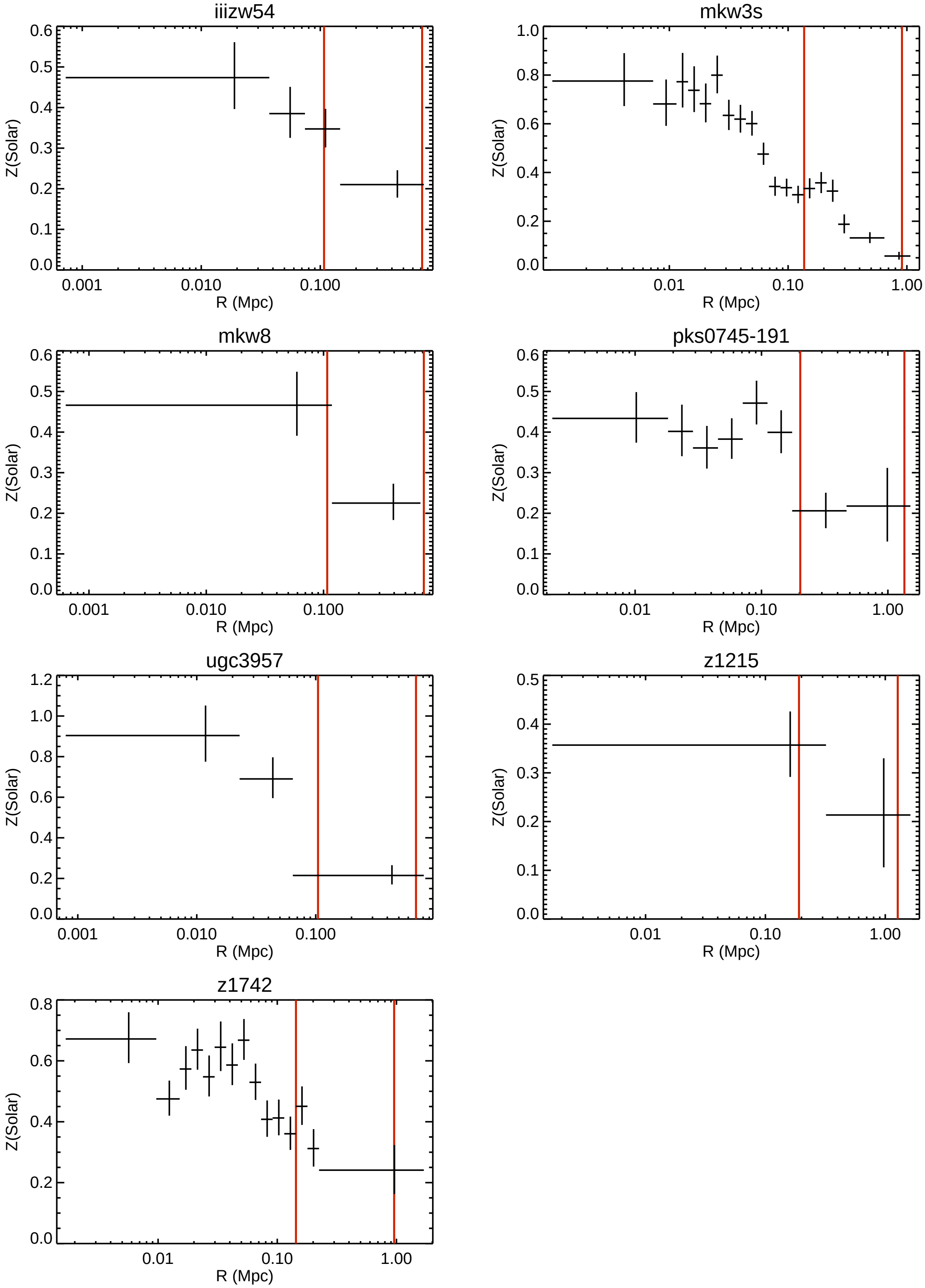

FIG. B1: *Continued.*

C. CLUSTER MASSES AND SCALES

TABLE C1: Cluster Masses and Scales.

Cluster	kT_X(keV)	R_{500}(Mpc)	$M_{500}(10^{14}M_\odot)$	$M_{gas}(10^{13}M_\odot)$
Abell 119	$5.79^{+0.1}_{-0.1}$	$1.13^{+0.02}_{-0.02}$	$4.46^{+0.2}_{-0.2}$	$4.50^{+0.1}_{-0.1}$
Abell 1413	$8.42^{+0.1}_{-0.2}$	$1.31^{+0.007}_{-0.03}$	$7.64^{+0.1}_{-0.6}$	$8.11^{+0.1}_{-0.2}$
Abell 1644	$5.31^{+0.05}_{-0.09}$	$1.15^{+0.02}_{-0.02}$	$4.78^{+0.3}_{-0.3}$	$5.50^{+0.2}_{-0.3}$
Abell 1651	$7.52^{+0.4}_{-0.3}$	$1.28^{+0.01}_{-0.03}$	$6.81^{+0.2}_{-0.5}$	$7.30^{+0.2}_{-0.2}$
Abell 1689	$10.4^{+0.2}_{-0.2}$	$1.45^{+0.005}_{-0.05}$	$10.9^{+0.1}_{-1.}$	$12.4^{+0.1}_{-0.4}$
Abell 1736	$3.19^{+0.05}_{-0.09}$	$0.920^{+0.03}_{-0.009}$	$2.43^{+0.3}_{-0.07}$	$2.80^{+0.2}_{-0.1}$
Abell 1795	$6.75^{+0.05}_{-0.05}$	$1.23^{+0.01}_{-0.02}$	$5.86^{+0.2}_{-0.3}$	$6.19^{+0.1}_{-0.1}$
Abell 1914	$10.1^{+0.5}_{-0.5}$	$1.45^{+0.004}_{-0.05}$	$10.7^{+0.1}_{-1.}$	$12.3^{+0.2}_{-0.5}$
Abell 2029	$8.20^{+0.09}_{-0.09}$	$1.44^{+0.06}_{-0.08}$	$9.60^{+1.}_{-1.}$	$12.5^{+2.}_{-3.}$
Abell 2063	$3.45^{+0.08}_{-0.09}$	$0.906^{+0.03}_{-0.009}$	$2.31^{+0.07}_{-0.2}$	$2.36^{+0.07}_{-0.06}$
Abell 2065	$6.18^{+0.2}_{-0.2}$	$1.19^{+0.02}_{-0.02}$	$5.36^{+0.2}_{-0.3}$	$5.80^{+0.1}_{-0.1}$
Abell 2142	$11.2^{+0.3}_{-0.3}$	$1.57^{+0.01}_{-0.06}$	$12.6^{+0.2}_{-1.}$	$14.5^{+0.1}_{-0.6}$
Abell 2147	$4.56^{+0.1}_{-0.1}$	$1.03^{+0.03}_{-0.009}$	$3.37^{+0.07}_{-0.3}$	$3.44^{+0.1}_{-0.08}$
Abell 2163	$23.4^{+1.}_{-1.}$	$2.14^{+0.07}_{-0.1}$	$35.1^{+4.}_{-6.}$	$43.2^{+2.}_{-4.}$
Abell 2204	$9.47^{+0.3}_{-0.3}$	$1.47^{+0.005}_{-0.06}$	$11.0^{+0.1}_{-1.}$	$13.6^{+0.2}_{-0.6}$
Abell 2244	$5.88^{+0.1}_{-0.1}$	$1.18^{+0.02}_{-0.02}$	$5.31^{+0.2}_{-0.3}$	$6.04^{+0.2}_{-0.2}$
Abell 2256	$7.73^{+0.3}_{-0.3}$	$1.37^{+0.03}_{-0.03}$	$8.11^{+0.5}_{-0.6}$	$9.54^{+0.8}_{-0.9}$
Abell 2319	$10.1^{+0.3}_{-0.2}$	$1.58^{+0.01}_{-0.06}$	$12.5^{+0.3}_{-1.}$	$15.6^{+0.3}_{-0.7}$
Abell 2657	$3.82^{+0.1}_{-0.1}$	$0.902^{+0.004}_{-0.03}$	$2.28^{+0.04}_{-0.2}$	$2.08^{+0.05}_{-0.07}$
Abell 2734	$4.28^{+0.2}_{-0.2}$	$0.982^{+0.03}_{-0.007}$	$3.00^{+0.05}_{-0.3}$	$3.02^{+0.1}_{-0.08}$
Abell 3112	$5.01^{+2.}_{-1.}$	$1.09^{+0.02}_{-0.02}$	$4.19^{+0.2}_{-0.2}$	$4.81^{+0.1}_{-0.1}$
Abell 3158	$5.20^{+0.06}_{-0.05}$	$1.10^{+0.02}_{-0.01}$	$4.23^{+0.2}_{-0.1}$	$4.53^{+0.08}_{-0.05}$
Abell 3376	$4.58^{+0.1}_{-0.1}$	$0.964^{+0.03}_{-0.002}$	$2.80^{+0.03}_{-0.2}$	$2.49^{+0.08}_{-0.02}$
Abell 3391	$5.41^{+0.4}_{-0.2}$	$1.10^{+0.02}_{-0.02}$	$4.19^{+0.3}_{-0.2}$	$4.28^{+0.1}_{-0.1}$
Abell 3571	$7.73^{+0.3}_{-0.3}$	$1.35^{+0.01}_{-0.03}$	$7.60^{+0.2}_{-0.5}$	$8.43^{+0.2}_{-0.2}$
Abell 3667	$6.60^{+0.01}_{-0.08}$	$1.32^{+0.01}_{-0.03}$	$7.33^{+0.2}_{-0.5}$	$9.38^{+0.4}_{-0.3}$
Abell 3822	$5.36^{+0.3}_{-0.2}$	$1.15^{+0.02}_{-0.02}$	$4.82^{+0.2}_{-0.3}$	$5.57^{+0.2}_{-0.2}$
Abell 3827	$7.89^{+0.2}_{-0.2}$	$1.33^{+0.01}_{-0.04}$	$7.60^{+0.3}_{-0.6}$	$8.46^{+0.3}_{-0.4}$
Abell 3921	$5.93^{+0.2}_{-0.2}$	$1.18^{+0.02}_{-0.02}$	$5.39^{+0.2}_{-0.3}$	$6.15^{+0.2}_{-0.1}$
Abell 399	$6.47^{+0.1}_{-0.1}$	$1.26^{+0.01}_{-0.03}$	$6.33^{+0.2}_{-0.4}$	$7.43^{+0.1}_{-0.2}$
Abell 400	$2.15^{+0.05}_{-0.04}$	$0.678^{+0.02}_{-0.04}$	$0.955^{+0.07}_{-0.2}$	$0.799^{+0.03}_{-0.07}$
Abell 4038	$3.12^{+0.05}_{-0.03}$	$0.839^{+0.008}_{-0.03}$	$1.82^{+0.05}_{-0.2}$	$1.71^{+0.04}_{-0.09}$
Abell 4059	$4.34^{+0.1}_{-0.02}$	$0.948^{+0.03}_{-0.004}$	$2.66^{+0.2}_{-0.03}$	$2.41^{+0.05}_{-0.07}$
Abell 478	$7.65^{+0.2}_{-0.2}$	$1.39^{+0.006}_{-0.04}$	$8.80^{+0.1}_{-0.7}$	$11.3^{+0.4}_{-0.2}$
Abell 539	$2.59^{+0.04}_{-0.04}$	$0.803^{+0.01}_{-0.03}$	$1.59^{+0.05}_{-0.2}$	$1.63^{+0.1}_{-0.03}$
Abell 644	$8.49^{+0.2}_{-0.1}$	$1.30^{+0.02}_{-0.03}$	$7.06^{+0.3}_{-0.5}$	$6.86^{+0.3}_{-0.3}$
Abell 754	$11.8^{+0.7}_{-0.2}$	$1.33^{+0.05}_{-0.04}$	$7.44^{+0.8}_{-0.8}$	$5.38^{+1.}_{-0.8}$
Abell S 405	$4.62^{+0.3}_{-0.3}$	$0.985^{+0.03}_{-0.007}$	$3.03^{+0.07}_{-0.3}$	$2.85^{+0.09}_{-0.1}$
Hydra A	$3.75^{+0.04}_{-0.03}$	$1.02^{+0.03}_{-0.008}$	$3.36^{+0.08}_{-0.2}$	$4.20^{+0.07}_{-0.1}$
Zw III 54	$2.25^{+0.06}_{-0.06}$	$0.718^{+0.01}_{-0.04}$	$1.14^{+0.07}_{-0.2}$	$1.05^{+0.03}_{-0.09}$
MKW 3s	$3.44^{+0.09}_{-0.03}$	$0.909^{+0.004}_{-0.03}$	$2.35^{+0.03}_{-0.2}$	$2.43^{+0.03}_{-0.1}$
MKW 8	$2.50^{+0.1}_{-0.1}$	$0.716^{+0.02}_{-0.04}$	$1.13^{+0.07}_{-0.2}$	$0.924^{+0.05}_{-0.07}$
PKS 0745-191	$6.76^{+0.5}_{-0.2}$	$1.35^{+0.01}_{-0.04}$	$8.09^{+0.2}_{-0.6}$	$11.1^{+0.4}_{-0.4}$
UGC 3957	$2.34^{+0.2}_{-0.1}$	$0.697^{+0.02}_{-0.04}$	$1.05^{+0.07}_{-0.2}$	$0.864^{+0.05}_{-0.05}$
ZwCl 1215+0400	$7.57^{+0.3}_{-0.3}$	$1.27^{+0.01}_{-0.03}$	$6.57^{+0.2}_{-0.5}$	$6.78^{+0.2}_{-0.2}$
ZwCl 1742+3306	$4.46^{+0.1}_{-0.1}$	$0.957^{+0.03}_{-0.006}$	$2.81^{+0.06}_{-0.2}$	$2.61^{+0.07}_{-0.08}$

D. DENSITY AND TEMPERATURE PROFILES BEST-FIT PARAMETERS

TABLE D1: Best-fit parameters of the electron density radial profiles.

Cluster	n_0	α	β	r_c	r_s	ϵ
Abell 119	0.0005406	0.627	5.0	2.959	0.289	1.227
Abell 1413	0.04096	0.0	0.3753	0.0217	0.3968	2.13
Abell 1644	0.04399	0.9245	0.3237	0.004989	2.17	5.0
Abell 1651	0.009126	0.6828	0.3982	0.08472	0.2506	1.249
Abell 1689	0.04991	0.0	0.399	0.0306	0.3455	1.99

Note. — Table D1 is published in its entirety in the electronic edition of the Astrophysical Journal. A portion is shown here for guidance regarding its form and content. The $n_e(r)$ model is shown in Equation 1.

TABLE D2: Best-fit parameters of the temperature radial profiles.

Cluster	r_t	a	b	c	a_{cool}	r_{cool}	t_{min}	t_0
Abell 119	0.2912	-0.3165	4.758	1.011	12.51	0.08264	19.22	8.419
Abell 1413	0.01754	0.4569	6.889	-0.7317	-0.7636	0.1653	1.329	7.881
Abell 1644	0.4703	-0.2443	7.74	0.5485	3.737	0.02752	4.614	6.027
Abell 1651	0.04094	0.04568	4.947	-0.0793	1.9	0.05	6.693	6.858
Abell 1689	1.046	-0.002614	7.542	3.02	8.231	0.07014	10.04	11.45

Note. — Table D2 is published in its entirety in the electronic edition of the Astrophysical Journal. A portion is shown here for guidance regarding its form and content. The $kT(r)$ model is shown in Equation 5.

E. MORPHOLOGICAL PARAMETERS

TABLE E1: Morphological Parameters and Entropy near the Center.

Cluster	c_{SB}[a]	S_{40}[b](keV cm^2)	$\langle w \rangle$[c]/10^{-3}
Abell 119	2.17± 0.037	$550.^{+69.}_{-65.}$	1.12
Abell 1413	9.91± 0.079	$112.^{+4.0}_{-3.7}$	0.607
Abell 1644	6.13± 0.057	$95.4^{+2.6}_{-2.1}$	(4.60)
Abell 1651	7.71± 0.16	$140.^{+4.2}_{-4.0}$	3.15
Abell 1689	12.3± 0.064	$108.^{+2.8}_{-2.4}$	1.16

Note. — Table E1 is published in its entirety in the electronic edition of the Astrophysical Journal. A portion is shown here for guidance regarding its form and content. Values of $\langle w \rangle$ in parentheses correspond to measurements in observations where the FOV does not fully cover the region $r < 0.3R_{500}$, and are excluded from analysis involving $\langle w \rangle$, but shown here.

[a] Surface brightness concentration.
[b] Entropy at r =40 kpc.
[c] Centroid shift.

F. GLOBAL METALLICITY MEASURES

TABLE F1: Global metallicity measures.

Cluster	$\bar{Z}_{mid}(Z_\odot)$	$\bar{Z}_{in}(Z_\odot)$
Abell 119	$0.260^{+0.036}_{-0.035}$	$0.337^{+0.047}_{-0.045}$
Abell 1413	$0.253^{+0.032}_{-0.032}$	$0.372^{+0.027}_{-0.026}$
Abell 1644	$0.226^{+0.029}_{-0.028}$	$0.360^{+0.028}_{-0.026}$
Abell 1651	$0.348^{+0.081}_{-0.076}$	$0.385^{+0.069}_{-0.064}$
Abell 1689	$0.304^{+0.032}_{-0.031}$	$0.352^{+0.025}_{-0.024}$
Abell 1736	$0.283^{+0.036}_{-0.034}$	$0.306^{+0.046}_{-0.044}$
Abell 1795	$0.240^{+0.023}_{-0.023}$	$0.324^{+0.013}_{-0.013}$
Abell 1914	$0.314^{+0.095}_{-0.091}$	$0.404^{+0.064}_{-0.061}$
Abell 2029	$0.238^{+0.024}_{-0.023}$	$0.421^{+0.015}_{-0.015}$
Abell 2063	$0.187^{+0.024}_{-0.022}$	$0.327^{+0.022}_{-0.021}$
Abell 2065	$0.221^{+0.043}_{-0.040}$	$0.316^{+0.041}_{-0.039}$
Abell 2142	$0.366^{+0.037}_{-0.036}$	$0.328^{+0.023}_{-0.022}$
Abell 2147	$0.290^{+0.038}_{-0.036}$	$0.269^{+0.039}_{-0.037}$
Abell 2163	$0.476^{+0.10}_{-0.10}$	$0.345^{+0.077}_{-0.075}$
Abell 2204	$0.397^{+0.043}_{-0.042}$	$0.391^{+0.025}_{-0.024}$
Abell 2244	$0.201^{+0.026}_{-0.025}$	$0.298^{+0.021}_{-0.020}$
Abell 2256	$0.289^{+0.086}_{-0.078}$	$0.389^{+0.065}_{-0.061}$
Abell 2319	$0.286^{+0.052}_{-0.050}$	$0.377^{+0.049}_{-0.047}$
Abell 2657	$0.281^{+0.043}_{-0.040}$	$0.460^{+0.055}_{-0.051}$
Abell 2734	$0.227^{+0.056}_{-0.052}$	$0.227^{+0.056}_{-0.052}$
Abell 3112	$0.182^{+0.034}_{-0.032}$	$0.394^{+0.029}_{-0.027}$
Abell 3158	$0.389^{+0.026}_{-0.024}$	$0.420^{+0.029}_{-0.027}$
Abell 3376	$0.312^{+0.042}_{-0.040}$	$0.225^{+0.044}_{-0.042}$
Abell 3391	$0.228^{+0.069}_{-0.064}$	$0.228^{+0.069}_{-0.064}$
Abell 3571	$0.191^{+0.034}_{-0.032}$	$0.392^{+0.024}_{-0.023}$
Abell 3667	$0.309^{+0.010}_{-0.010}$	$0.345^{+0.012}_{-0.011}$
Abell 3822	$0.258^{+0.067}_{-0.063}$	$0.258^{+0.067}_{-0.063}$
Abell 3827	$0.265^{+0.052}_{-0.049}$	$0.368^{+0.038}_{-0.036}$
Abell 3921	$0.327^{+0.051}_{-0.049}$	$0.308^{+0.041}_{-0.039}$
Abell 399	$0.283^{+0.047}_{-0.045}$	$0.307^{+0.049}_{-0.046}$
Abell 400	$0.394^{+0.040}_{-0.036}$	$0.548^{+0.059}_{-0.053}$
Abell 4038	$0.355^{+0.025}_{-0.023}$	$0.440^{+0.020}_{-0.019}$
Abell 4059	$0.250^{+0.017}_{-0.016}$	$0.466^{+0.013}_{-0.012}$
Abell 478	$0.257^{+0.025}_{-0.024}$	$0.328^{+0.016}_{-0.015}$
Abell 539	$0.212^{+0.023}_{-0.021}$	$0.225^{+0.024}_{-0.022}$
Abell 644	$0.323^{+0.044}_{-0.042}$	$0.438^{+0.038}_{-0.036}$
Abell 754	$0.302^{+0.058}_{-0.057}$	$0.369^{+0.036}_{-0.035}$
Abell S 405	$0.264^{+0.083}_{-0.077}$	$0.264^{+0.083}_{-0.077}$
Hydra A	$0.147^{+0.0095}_{-0.0094}$	$0.236^{+0.0055}_{-0.0054}$
Zw III 54	$0.258^{+0.029}_{-0.026}$	$0.370^{+0.037}_{-0.034}$
MKW 3s	$0.328^{+0.025}_{-0.024}$	$0.395^{+0.017}_{-0.017}$
MKW 8	$0.241^{+0.045}_{-0.039}$	$0.466^{+0.082}_{-0.075}$
PKS 0745-191	$0.206^{+0.045}_{-0.043}$	$0.369^{+0.028}_{-0.026}$
UGC 3957	$0.215^{+0.051}_{-0.044}$	$0.426^{+0.049}_{-0.043}$
ZwCl 1215+0400	$0.315^{+0.060}_{-0.056}$	$0.357^{+0.069}_{-0.065}$
ZwCl 1742+3306	$0.314^{+0.045}_{-0.042}$	$0.447^{+0.026}_{-0.025}$